d → f Energy Transfer in a Series of Ir[III]/Eu[III] Dyads: Energy-Transfer Mechanisms and White-Light Emission[†]

Daniel Sykes,[‡] Ian S. Tidmarsh,[‡] Andrea Barbieri,[§] Igor V. Sazanovich,[‡] Julia A. Weinstein,[‡] and Michael D. Ward*,[‡]

[‡]Department of Chemistry, University of Sheffield, Sheffield S3 7HF, U.K.
[§]Istituto ISOF—CNR, Via P. Gobetti 101, 40129 Bologna, Italy

S *Supporting Information*

ABSTRACT: An extensive series of blue-luminescent iridium(III) complexes has been prepared containing two phenylpyridine-type ligands and one ligand containing two pyrazolylpyridine units, of which one is bound to Ir[III] and the second is pendant. Attachment of {Ln(hfac)$_3$} (Ln = Eu, Gd; hfac = anion of 1,1,1,5,5,5,-hexafluoro-pentanedione) to the second coordination site affords Ir[III]/Ln[III] dyads. Crystallographic analysis of several mononuclear iridium(III) complexes and one Ir[III]/Eu[III] dyad reveals that in most cases the complexes can adopt a folded conformation involving aromatic π stacking between a phenylpyridine ligand and the bis(pyrazolylpyridine) ligand, but in one series, based on CF$_3$-substituted phenylpyridine ligands coordinated to Ir[III], the steric bulk of the CF$_3$ group prevents this and a quite different and more open conformation arises. Quantum mechanical calculations well reproduce these two types of "folded" and "open" conformations. In the Ir[III]/Eu[III] dyads, Ir → Eu energy transfer occurs with varying degrees of efficiency, resulting in partial quenching of the Ir[III]-based blue emission and the appearance of a sensitized red emission from Eu[III]. Calculations based on consideration of spectroscopic overlap integrals rule out any significant contribution from Förster (dipole—dipole) energy transfer over the distances involved but indicate that Dexter-type (exchange) energy transfer is possible if there is a small electronic coupling that would arise, in part, through π stacking between components. In some cases, an initial photoinduced *electron*-transfer step could also contribute to Ir → Eu energy transfer, as shown by studies on isostructural iridium/gadolinium model complexes. A balance between the blue (Ir-based) and red (Eu-based) emission components can generate white light.
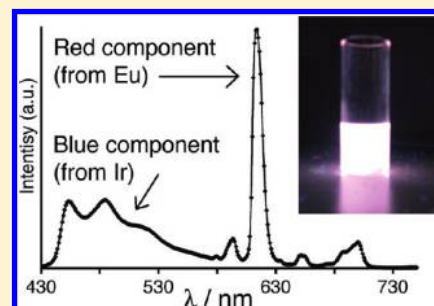
■ INTRODUCTION

In recent years, the use of transition-metal (d-block) chromophores as antenna groups to generate sensitized luminescence from lanthanide(III) ions in d/f dyads has attracted substantial attention from several research groups.[1−4] Transition-metal chromophores, especially polypyridyl complexes of d^6 (e.g., Ru[II], Os[II], Re[I]) and d^8 (especially Pt[II]) metal ions, have many desirable properties for use as energy donors to lanthanides instead of the more usual organic chromophores. These advantages include (i) intense absorption arising from fully allowed low-energy charge-transfer bands, with a maximum that can be selected to be almost anywhere in the UV/vis/near-IR region, (ii) long-lived excited states, often of triplet metal-to-ligand charge-transfer (^{3}MLCT) character, which maximize the likelihood of energy transfer to the Ln[III] ion, (iii) photochemical stability and kinetic inertness, and (iv) luminescence of their own, which provides a basis to monitor energy transfer to the lanthanide(III) acceptor.[1,2] The majority of the work in this area has involved Ln[III] ions with low-energy excited states that emit in the near-IR region (Nd[III], Yb[III], Er[III], and Pr[III]), which is of considerable interest given the relevance of near-IR luminescence to areas as diverse as biological imaging and telecommunications. In some Ru[II]/Nd[III] dyads, we showed recently that Ru → Nd energy transfer, resulting in sensitized

Nd-based emission, could occur by a Dexter-type mechanism over a distance of 20 Å, facilitated by a long-conjugated oligo-(phenylene) spacer in the bridging ligand.[4]

Generating sensitized luminescence from visible-emitting lanthanides such as Eu[III] is, however, more challenging in d/f dyads because the higher energy of the emissive excited states (^{5}D$_0$, ca. 17 300 cm^{-1}) requires the use of transition-metal chromophores as sensitizers, which themselves have a sufficiently high-energy excited state to act as the energy donors. For the excited state of a d-block complex to act as an energy donor to Eu[III], it must lie at least 1700 cm^{-1} above the ^{5}D$_0$ level to prevent thermally activated back energy transfer at room temperature.[5] This requires an excited-state energy of >19 000 cm^{-1} for the donor. If a higher-lying excited state of Eu[III] is populated as a result of selection rule restrictions on energy transfer (see later), then the donor must have an even higher energy content. Thus, the energies required are considerably higher than is accessible with the usual d^6 or d^8 metal complexes mentioned earlier; e.g., [Ru(bipy)$_3$]$^{2+}$ (bipy = 2,2′-bipyridine) has a ^{3}MLCT energy of ca. 17 000 cm^{-1}. However, much recent work on luminescent

Chart 1
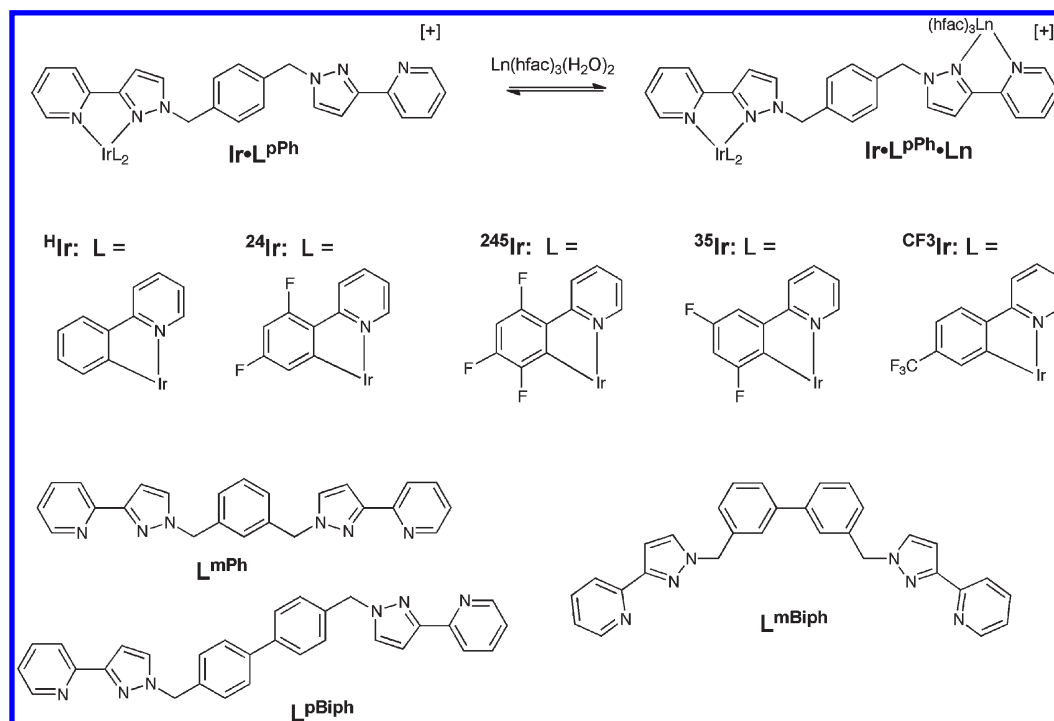
iridium(III) complexes based on cyclometallating phenylpyridine-type ligands has shown that, with judicious choice of ligands and substituents, blue-emitting complexes with excited-state energies well in excess of 19 000 cm^{-1} can be prepared;[6,7] this has been driven principally by their possible use in organic light-emitting devices. These are ideal candidates for use in d/f dyads to generate sensitized emission from Eu^{III}.

The use of iridium(III) complexes as energy donors in d/f dyads has received relatively little attention,[3] despite their ease of synthesis and the straightforward tunability of the absorption/emission properties over a wide range; in many of these cases, the Ln^{III} unit is a near-IR emitter rather than a visible emitter such as Eu^{III}.[3a−c] In this paper, we report the syntheses, structures, and photophysical properties of a series of Ir^{III}/Eu^{III} dyads that display Ir → Eu photoinduced energy transfer (hereafter abbreviated as "PEnT" to avoid confusion with "PET", which is commonly used for photoinduced electron transfer), and we analyze the structural properties that are responsible for differing degrees of PEnT in the complexes.

Our interest in these is driven by possible applications in two areas. First, if the extent of d → f energy transfer can be controlled in these dyads, we can control the relative contributions of the d-block emission (Ir, blue to green) and the Eu^{III} emission (red), such that white-light emission can be generated from a single molecule using a balance of blue/green and red luminescence components, as demonstrated by De Cola et al. with an Ir^{III}/Eu^{III} dyad[3e] and by other groups using different combinations of red and blue emitters.[8] Second, the widespread use of Eu^{III} emission in biological assays and for imaging purposes[9] requires that its emission be sensitized at wavelengths that are nondestructive to biological samples, which means that UV excitation should be avoided. The use of these iridium(III) chromophores as energy donors allows relatively low-energy excitation in the visible region of the spectrum to be used. Additionally, the recent demonstration

that iridium(III) complexes of this nature can be excited by a two-photon process using near-IR excitation at 800 nm opens up the possibility of using low-energy excitation—at wavelengths where biological samples are relatively transparent—to excite the iridium(III) chromophore and hence generate the important Eu^{III}-based emission.[10]

■ RESULTS AND DISCUSSION

Design and Synthesis of Iridium(III) Complexes. To prepare the Ir^{III}/Ln^{III} dyads, we required a series of bridging ligands in which (i) the terminus binding to Ir^{III} helps to generate the desired high-energy excited state and (ii) the other terminus binds to Ln^{III} ions with high affinity. These criteria are well met by the series of bridging ligands shown in Chart 1, which comprise two pyrazolylpyridine chelating units attached to a central aromatic spacer; conveniently, these ligands were available from different work in which they have been used as the basis of the self-assembly of polyhedral coordination cages with transition-metal ions.[11] Complexes based on {Ir(phpy)$_2$}$^+$ fragments (Hphpy = 2-phenylpyridine) but also containing five-membered nitrogen-rich heterocycles in their coordination sphere, such as triazole and pyrazole donors, have high-energy luminescence due to the high-energy lowest unoccupied molecular orbital (LUMO) of the azole ligand.[6,7] The use of fluorinated phenylpyridine derivatives conversely stabilizes the highest occupied molecular orbital (HOMO; which is a combination of both Ir and phpy components). Thus, the use of fluorinated phpy derivatives in the {Ir(phpy)$_2$}$^+$ core, and a pyrazolylpyridine unit as the other chelating fragment, results in a high HOMO/LUMO gap and luminescence at the blue end of the visible spectrum.[6,7] The second N,N-chelating terminus of the bridging ligand binds to {Ln(diketonate)$_3$} fragments by displacing two water ligands from [Ln(diketonate)$_3$(H$_2$O)$_2$] units to generate an eight-coordinate

Table 1. Crystal Parameters, Data Collection, and Refinement Details for the Structures in This Paper

complex	$[^{24}\mathbf{Ir}\cdot L^{pPh}]\cdot CH_2Cl_2$	$[^{245}\mathbf{Ir}\cdot L^{pPh}]\cdot CHCl_3\cdot 0.5H_2O$	$[^{35}\mathbf{Ir}\cdot L^{pPh}]\cdot CH_2Cl_2$
formula	$C_{47}H_{34}Cl_2F_4IrN_9O_3{}^b$	$C_{47}H_{32}Cl_3F_6IrN_9O_{3.5}{}^b$	$C_{47}H_{34}Cl_2F_4IrN_9O_3{}^b$
mol wt	1111.93	1191.37	1111.93
T, K	150(2)	150(2)	150(2)
cryst syst	triclinic	triclinic	monoclinic
space group	$P\bar{1}$	$P\bar{1}$	$P2_1/c$
a, Å	9.9873(3)	14.2790(19)	21.2697(7)
b, Å	14.3280(5)	19.232(4)	11.2972(3)
c, Å	16.9827(6)	19.724(3)	18.2126(5)
α, deg	113.757(2)	105.895(2)	90
β, deg	90.314(2)	110.582(2)	94.062(2)
γ, deg	93.876(2)	106.298(2)	90
V, Å^3	2217.75(13)	4428.8(13)	4365.3
Z	2	4	4
ρ, g cm^{-3}	1.665	1.787	1.692
cryst size, mm^3	0.75 × 0.13 × 0.12	0.44 × 0.10 × 0.03	0.30 × 0.27 × 0.02
μ, mm^{-1}	3.201	3.278	3.253
data, restraints, param	10 123/15/604	19 972/181/1192	7439/59/604
final R1, wR2^a	0.0509, 0.1440	0.0574, 0.1590	0.0428, 0.1179

complex	$[^{24}\mathbf{Ir}\cdot L^{mBiph}]\cdot 2.5CHCl_3{}^b$	$[^{24}\mathbf{Ir}\cdot L^{pBiph}]\cdot CHCl_3\cdot H_2O{}^b$	$[^{24}\mathbf{Ir}\cdot L^{mPh}]\cdot CH_2Cl_2{}^c$
formula	$C_{54.5}H_{38.5}Cl_{7.5}F_4IrN_9O_3$	$C_{53}H_{39}Cl_3F_4IrN_9O_4$	$C_{47}H_{34}Cl_2F_{10}IrN_8P$
mol wt	1401.52	1240.48	1194.89
T, K	150(2)	100(2)	150(2)
cryst syst	monoclinic	monoclinic	triclinic
space group	$P2_1/n$	$P2_1/c$	$P\bar{1}$
a, Å	15.7829(7)	19.1604(7)	11.1126(3)
b, Å	20.9113(8)	12.2450(4)	13.4765(3)
c, Å	18.3348(7)	23.0661(9)	15.7590(4)
α, deg	90	90	93.0620(10)
β, deg	104.315(2)	113.843(2)	103.4640(10)
γ, deg	90	90	92.7780(10)
V, Å^3	5863.3(4)	4949.9(3)	2287.40(10)
Z	4	4	2
ρ, g cm^{-3}	1.588	1.665	1.735
cryst size, mm^3	0.28 × 0.27 × 0.23	0.35 × 0.22 × 0.09	0.20 × 0.15 × 0.10
μ, mm^{-1}	2.682	2.392	3.156
data, restraints, param	13 426/88/716	11 017/4/667	10 217/1082/745
final R1, wR2^a	0.0777, 0.2527	0.0458, 0.1480	0.0380, 0.1080

complex	$[^{CF3}\mathbf{Ir}\cdot L^{mPh}]\cdot CH_2Cl_2\cdot 0.5H_2O{}^c$	$[^{245}\mathbf{Ir}\cdot L^{pPh}\cdot\mathbf{Eu}]\cdot CH_2Cl_2{}^d$
formula	$C_{49}H_{37}Cl_2F_{12}IrN_8O_{0.5}P$	$C_{82}H_{39}Cl_2Eu_2F_{48}IrN_8O_{14}$
mol wt	1267.94	2839.23
T, K	150(2)	150(2)
cryst syst	monoclinic	triclinic
space group	$P2_1/n$	$P\bar{1}$
a, Å	19.0934(18)	13.7794(12)
b, Å	13.1480(12)	19.1574(17)
c, Å	21.542(2)	19.4502(17)
α, deg	90	93.6220(10)
β, deg	114.288(4)	92.0430(10)
γ, deg	90	106.0270(10)
V, Å^3	4929.2(8)	4916.7(7)
Z	4	2
ρ, g cm^{-3}	1.709	1.918
cryst size, mm^3	0.20 × 0.15 × 0.12	0.50 × 0.26 × 0.18
μ, mm^{-1}	2.941	2.819
data, restraints, param	8416/578/665	22 185/141/1396
final R1, wR2^a	0.0716, 0.2218	0.0485, 0.1373

^{a} The value of R1 is based on "observed" data with $I > 2\sigma(I)$; the value of wR2 is based on all data. ^{b} The anion is nitrate. ^{c} The anion is hexafluorophosphate. ^{d} The anion is $[Eu(hfac)_4]^-$.

[Ln(diketonate)$_3$(NN)] complex with a high binding constant in a noncompetitive solvent such as CH$_2$Cl$_2$ (see Chart 1 for an example).[1a,3f,3g,4]

The mononuclear iridium(III) "complex ligands" were simply prepared in good yield by reaction of the appropriate [Ir(phpy)$_2$-(μ-Cl)]$_2$ dimer with 2 equiv of the appropriate bridging ligand L in a 1:2 ratio such that the Ir:L ratio was 1:1. Chromatographic purification separated the desired mononuclear complexes from traces of the unwanted dinuclear complexes; the products were isolated as their nitrate salts and were readily soluble in CH$_2$Cl$_2$ and other polar organic solvents. All complexes were satisfactorily characterized by ^{1}H NMR spectroscopy, mass spectrometry, and elemental analyses, and many have been structurally characterized. The series of complexes prepared (Chart 1) covers a range of differently substituted phenylpyridine ligands to afford different excited-state energies for the Ir^{III} centers and different lengths and conformations of the bridging ligands to afford differing degrees of Ir → Eu PEnT.

A note on the nomenclature scheme is appropriate here. The Ir^{III} termini are denoted as ^{H}**Ir** (based on unsubstituted phenylpyridine ligands, i.e., bearing only H-atom substituents), ^{24}**Ir** [based on 2-(2,4-difluorophenyl)pyridine], ^{35}**Ir** [based on 2-(3,5-difluorophenyl)pyridine], ^{245}**Ir** [based on 2-(2,4,5-trifluorophenyl)pyridine], or ^{CF3}**Ir** {based on 2-[4-(trifluoromethyl)-phenyl]pyridine}. Terminal {Eu(hfac)$_3$} or {Gd(hfac)$_3$} units are denoted as **Eu** or **Gd**. The bridging ligands have the abbreviations shown in Chart 1 based on the nature of the aromatic spacer group. Thus, ^{24}**Ir·**L^{mPh} is the mononuclear complex [Ir{(2,4-F$_2$–C$_6$H$_3$)pyridine}$_2$(L^{mPh})](NO$_3$), and ^{24}**Ir·**L^{mPh}**·Eu** is the dinuclear adduct with a {Eu(hfac)$_3$} unit attached to the secondary pyrazolylpyridine site. We use **Ir** (with no superscript denoting substituents) as a generic label for all of the Ir^{III} units.

Structures of Mononuclear Iridium(III) Complexes. Several of the mononuclear complexes have been structurally characterized, and the structures will be grouped for discussion based on the nature of the bis(pyrazolylpyridine) ligand L (see Tables 1 and 2). Figure 1 shows the structures of three complexes containing L^{pPh} but with different substituents on the terminal phenylpyridine ligands, viz., ^{24}**Ir·**L^{pPh}, ^{245}**Ir·**L^{pPh}, and ^{35}**Ir·**L^{pPh}. Individual bond distances and angles around the Ir^{III} centers are unremarkable. The most interesting feature of these structures is that in every case the pendant phenyl ring of L^{pPh} is approximately orthogonal to the coordinated pyrazolylpyridine group from which it is pendant because of the torsion about the intervening methylene spacer. This allows the pendant phenyl ring, containing atoms C(151)−C(156), to lie approximately parallel to and stacked with the phenylpyridine ligand containing N(211) and C(221): angles between the phenyl and phenylpyridine mean planes are 7.9, 6.5, and 1.4°, respectively, and distances are in the range 3.1−3.6 Å between the atoms of one aromatic unit and the mean plane of the other. An alternative view of the structure of ^{24}**Ir·**L^{pPh} emphasizing this overlap is in Figure 1d. This stacking will be facilitated by the electron-deficient nature of the coordinated phpy ligand (due to the pyridine ring, the fluorine substituents, and coordination to Ir^{III}) and relies for steric reasons on the absence of out-of-plane bulky substituents on the phenylpyridine ligand; we return to this point later.

Figure 2 shows the structures of ^{24}**Ir·**L^{mBiph} and ^{24}**Ir·**L^{pBiph} in which the bis(pyrazolylpyridine) ligands have a biphenyl spacer separating the bidentate termini. Again, the first phenyl ring pendant from the coordinated pyrazolylpyridine group lies parallel to

Table 2. Selected Bond Distances (Å) for the Crystal Structures

^{24}**Ir·**L^{pPh}			
Ir(1)−C(221)	2.009(6)	Ir(1)−N(311)	2.036(5)
Ir(1)−C(321)	2.022(6)	Ir(1)−N(122)	2.150(5)
Ir(1)−N(211)	2.030(6)	Ir(1)−N(111)	2.167(5)
^{245}**Ir·**L^{pPh}			
Ir(1)−C(321)	2.005(8)	Ir(1)−N(211)	2.035(7)
Ir(1)−N(311)	2.013(7)	Ir(1)−N(111)	2.139(6)
Ir(1)−C(221)	2.034(7)	Ir(1)−N(122)	2.146(6)
^{35}**Ir·**L^{pPh}			
Ir(1)−C(321)	2.013(10)	Ir(1)−N(311)	2.058(8)
Ir(1)−C(221)	2.033(11)	Ir(1)−N(122)	2.126(7)
Ir(1)−N(211)	2.046(7)	Ir(1)−N(111)	2.140(7)
^{24}**Ir·**L^{mBiph}			
Ir(1)−C(221)	2.013(11)	Ir(1)−N(211)	2.056(8)
Ir(1)−C(321)	2.020(10)	Ir(1)−N(122)	2.155(8)
Ir(1)−N(311)	2.054(9)	Ir(1)−N(111)	2.165(9)
^{24}**Ir·**L^{pBiph}			
Ir(1)−C(41)	1.992(7)	Ir(1)−N(31)	2.054(6)
Ir(1)−C(21)	2.008(7)	Ir(1)−N(61)	2.158(5)
Ir(1)−N(11)	2.047(6)	Ir(1)−N(51)	2.169(5)
^{24}**Ir·**L^{mPh}			
Ir(1)−C(321)	2.000(5)	Ir(1)−N(311)	2.051(4)
Ir(1)−C(221)	2.015(5)	Ir(1)−N(122)	2.158(4)
Ir(1)−N(211)	2.049(4)	Ir(1)−N(111)	2.160(5)
^{CF3}**Ir·**L^{mPh}			
Ir(1)−C(321)	2.003(14)	Ir(1)−N(311)	2.051(11)
Ir(1)−C(221)	2.004(14)	Ir(1)−N(111)	2.149(11)
Ir(1)−N(211)	2.035(11)	Ir(1)−N(122)	2.178(11)
^{245}**Ir·**L^{pPh}**·Eu**			
Ir(1)−C(321)	2.015(6)	Eu(1)−O(623)	2.347(4)
Ir(1)−C(221)	2.029(6)	Eu(1)−O(422)	2.360(4)
Ir(1)−N(211)	2.044(5)	Eu(1)−O(622)	2.373(4)
Ir(1)−N(311)	2.051(5)	Eu(1)−O(522)	2.386(5)
Ir(1)−N(122)	2.146(5)	Eu(1)−O(423)	2.403(5)
Ir(1)−N(111)	2.147(4)	Eu(1)−N(131)	2.537(5)
Eu(1)−O(523)	2.336(4)	Eu(1)−N(142)	2.556(5)

and stacked with one of the fluorinated phenylpyridine ligands at the Ir^{III} center.

A comparison of the two structures obtained by incorporating L^{mPh} (Figure 3) is particularly revealing. We can see how this recurring π-stacking motif is made possible by the low steric demands of those phenylpyridine ligands containing 2,4-difluoro and 3,5-difluoro substituents on the phenyl ring; these ligands are planar, which facilitates the stacking interaction. Use instead of the bulkier CF$_3$ substituent prevents the close approach of another aromatic unit necessary for π stacking and so disrupts this interaction. Thus, Figure 3a shows the structure of ^{24}**Ir·**L^{mPh}, which follows the pattern that we have seen in all of the previous examples (Figures 1 and 2), with the phenylene spacer [containing atoms C(151)−C(156)] lying parallel to and stacked with the phenylpyridine ligand containing N(211) and C(221). In contrast, ^{CF3}**Ir·**L^{mPh} provides the one instance that we have
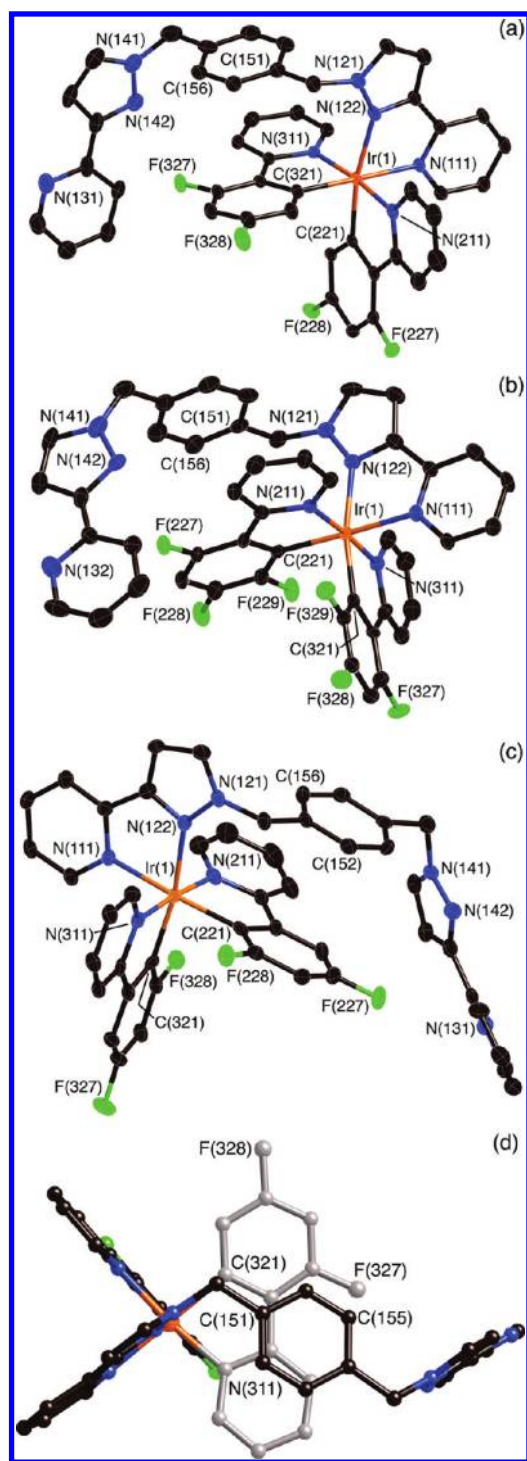
Figure 1. Molecular structures of the complex cations of (a) ^{24}**Ir**·L^{PPh}, (b) ^{245}**Ir**·L^{PPh}, and (c) ^{35}**Ir**·L^{PPh}. (d) Alternative view of the structure of ^{24}**Ir**·L^{PPh} emphasizing the overlap of the phenyl ring of L^{PPh} with one of the phenylpyridine ligands. Thermal ellipsoids are at the 30% probability level.

observed where this π stacking between the aromatic core of the pendant ligand and the {Ir(phpy)$_2$}$^+$ fragment does *not* occur because of the steric bulk of the CF$_3$ substituent (Figure 3b,c), with the pendant phenyl group of L^{mPh} now being oriented to avoid an unfavorable steric interaction. This is emphasized in Figure 3b, which shows how the phenyl ring C(151)−C(156) is
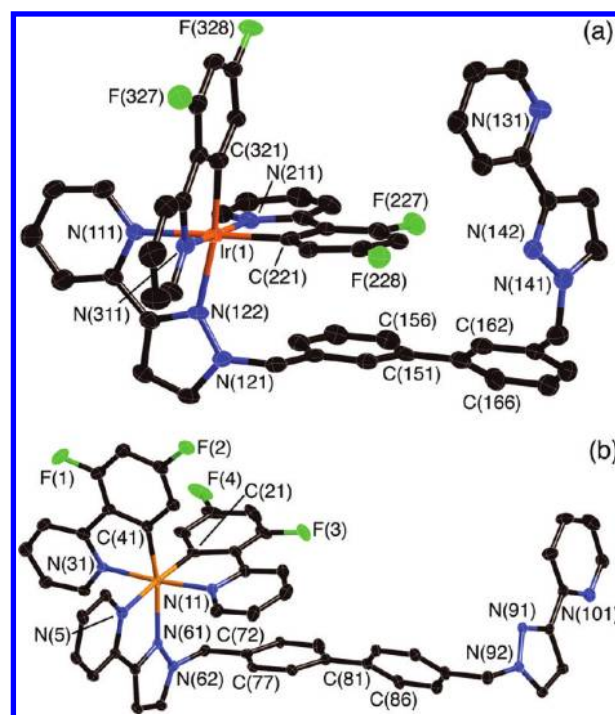
Figure 2. Molecular structures of the complex cations of (a) ^{24}**Ir**·L^{mBiph} and (b) ^{24}**Ir**·L^{PBiph}. Color scheme as for Figure 1. Thermal ellipsoids are at the 30% probability level.

conspicuously not stacked with the phpy ligand containing N(311) and C(321), with phenyl ring C(151)−C(156) and its pendant pyrazolylpyridine group folded back on itself in a manner quite different from what is observed in every other case. This has important consequences for energy transfer in Ir/Eu dyads based on the ^{CF3}**Ir** chromophore (see later).

Photophysical Properties of Mononuclear Iridium(III) Complexes. The photophysical properties of the iridium(III) complexes are summarized in Tables 3 (UV/vis absorption) and 4 (luminescence) and contain little that is unexpected based on the known properties of iridium(III) complexes that contain (i) phenylpyridine ligands with varying patters of F-atom substituents and (ii) a chelating pyridylpyrazole ligand, both factors of which combine to give a high-energy excited state and strong emission in the blue region of the spectrum. The UV/vis absorption spectra showed, in addition to the expected strong absorptions in the UV region associated with aromatic ligands, a less intense but still strong band (ε between 3200 and 9400 M^{-1} cm^{-1}) in the 360−410 nm region associated with the formation of the lowest-energy excited state that has a mixture of ligand-centered (LC) π−π^*, and MLCT, character.

The nature of the aromatic group pendant from the coordinated pyrazolylpyridine had a negligible effect such that all complexes with the same primary coordination sphere around Ir^{III} have very similar luminescence properties. Thus, we see that the series ^{H}**Ir**·L and ^{CF3}**Ir**·L have slightly longer emission wavelengths (477 and 481 nm, respectively) than the ^{24}**Ir**·L and ^{245}**Ir**·L series (455 and 452 nm, respectively); the change in the position of the F-atom substituents in the series ^{35}**Ir**·L shifts the emission maximum to 475 nm. All of the emission spectra showed the usual series of well-resolved vibrational components, with lifetimes (in aerated CH$_2$Cl$_2$) of ca. 200 ns for the ^{H}**Ir**·L series and in the region 700−1600 ns for all of the other series
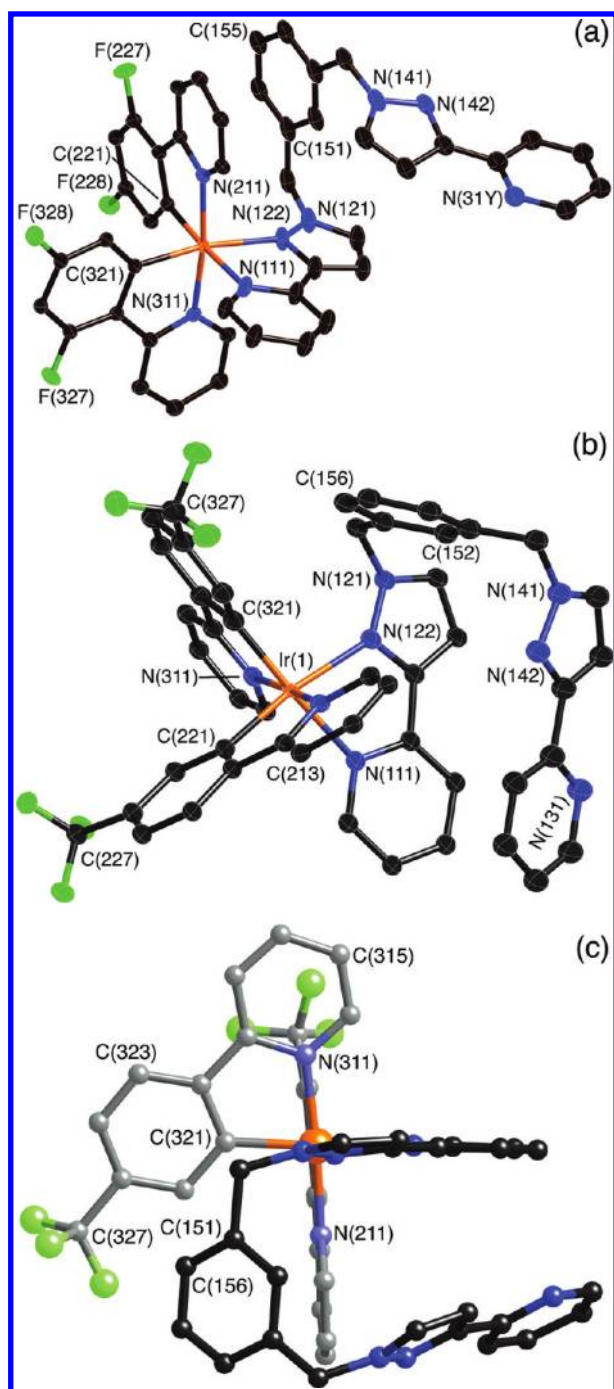
Figure 3. Molecular structures of the complex cations of (a) $^{24}\mathbf{Ir}\cdot L^{mPh}$ and (b) $^{CF3}\mathbf{Ir}\cdot L^{mPh}$. Color scheme as for Figure 1. (c) Alternative view of the structure of $^{CF3}\mathbf{Ir}\cdot L^{mPh}$ emphasizing how the steric bulk of the trifluormethyl group prevents aromatic stacking between the phenyl ring of L^{mPh} and the phenylpyridine ligands (cf. Figure 1d). Thermal ellipsoids are at the 30% probability level.

Table 3. Summary of UV/Vis Spectral Data for the Iridium-(III) Complexes in CH$_2$Cl$_2$

complex	λ_{max}/nm $(10^{-3}\varepsilon/M^{-1}\,cm^{-1})$
$^{H}\mathbf{Ir}\cdot L^{pPh}$	255 (58), 320 (14), 375 (4.9)
$^{H}\mathbf{Ir}\cdot L^{mPh}$	262 (69), 283 (53), 325 (18), 379 (9.4)
$^{H}\mathbf{Ir}\cdot L^{pBiph}$	259 (75), 338 (10), 379 (6.0), 407 (4.5)
$^{H}\mathbf{Ir}\cdot L^{mBiph}$	255 (71), 283 (43), 379 (5.0)
$^{24}\mathbf{Ir}\cdot L^{pPh}$	253 (58), 279 (39), 315 (16), 361 (5.6)
$^{24}\mathbf{Ir}\cdot L^{mPh}$	251 (56), 280 (40), 360 (6.2)
$^{24}\mathbf{Ir}\cdot L^{pBiph}$	258 (55), 284 (38), 320 (13), 363 (3.8)
$^{24}\mathbf{Ir}\cdot L^{mBiph}$	254 (57), 279 (35), 317 (11), 364 (4.1)
$^{245}\mathbf{Ir}\cdot L^{pPh}$	238 (53), 256 (55), 283 (35), 313 (21), 357 (4.4)
$^{245}\mathbf{Ir}\cdot L^{mBiph}$	239 (58), 256 (65), 313 (20), 359 (3.4)
$^{35}\mathbf{Ir}\cdot L^{pPh}$	259 (52), 287 (35), 318 (15), 379 (4.7)
$^{35}\mathbf{Ir}\cdot L^{mPh}$	258 (50), 284 (36), 317 (15), 375 (5.1)
$^{35}\mathbf{Ir}\cdot L^{pBiph}$	259 (45), 284 (31), 333 (5.9), 375 (3.1)
$^{CF3}\mathbf{Ir}\cdot L^{pPh}$	253 (58), 283 (39), 379 (4.9)
$^{CF3}\mathbf{Ir}\cdot L^{mPh}$	253 (58), 282 (40), 379 (4.9), 407 (3.2)
$^{CF3}\mathbf{Ir}\cdot L^{pBiph}$	258 (82), 286 (54), 340 (6.2), 382 (3.8)
$^{CF3}\mathbf{Ir}\cdot L^{mBiph}$	253 (78), 279 (45), 379 (6.6), 408 (4.5)

component in the excited state, which is destabilized when the solvent cannot repolarize to take account of the changed charge distribution. From the emission maxima at 77 K, it is clear that this series of complexes provides excited-state energies in the range 21 000—22 000 cm^{-1}, which should be more than sufficient to sensitize Eu^{III}. Although direct energy transfer to generate the $^5D_0$ level of Eu^{III} from the $^7F_0$ ground state is forbidden by the relevant selection rules (see the later discussion), there is more than enough excited-state energy available in these Ir^{III} fluorophores to sensitize higher-lying levels of Eu^{III} such as $^5D_1$, which can then generate the emissive $^5D_0$ level by internal conversion.

Syntheses of Ir/Ln Dyads and a Structurally Characterized Example. Preparation of the $\mathbf{Ir}\cdot L\cdot\mathbf{Ln}$ (Ln = Gd, Eu) dyads was achieved simply by combining the relevant $\mathbf{Ir}\cdot L$ mononuclear complex with Ln(hfac)$_3\cdot$2H$_2$O in a CH$_2$Cl$_2$ solution. Under these conditions, the equilibrium shown in Chart 1 occurs in which the chelating diimine ligand displaces the two water molecules to give an eight-coordinate Ln(hfac)$_3$(diimine) unit. To ensure that the reaction goes to completion (or very close to completion), an excess of Ln(hfac)$_3\cdot$2H$_2$O can be used in a spectroscopic titration; because our photophysical measurements all involved selective excitation of the Ir^{III}-based chromophore, the excess of unbound Ln(hfac)$_3\cdot$2H$_2$O present at the end of the spectroscopic titrations is effectively invisible and does not interfere with the results. This is a general approach that we have used before.[1a,3f,3g,4] In this case, we have used Eu(hfac)$_3\cdot$2H$_2$O to make the Ir/Eu dyads for the purpose of studying Ir $\rightarrow$ Eu PEnT, and we used Gd(hfac)$_3\cdot$2H$_2$O to make analogous Ir/Gd complexes as controls to see what effect (if any) the presence of a nonquenching {Ln(hfac)$_3$} unit had on the photophysical properties of the complexes.

Slow evaporation of a solution containing $^{245}\mathbf{Ir}\cdot L^{pPh}$ and excess Eu(hfac)$_3\cdot$2H$_2$O in CH$_2$Cl$_2$ afforded crystals of the dyad $^{245}\mathbf{Ir}\cdot L^{pPh}\cdot\mathbf{Eu}$ (Figure 5). Significantly, the general arrangement of the $^{245}\mathbf{Ir}\cdot L^{pPh}$ unit is not significantly changed (cf. Figure 1b), with the phenyl ring of the bridging ligand [C(151)—C(156)] lying parallel to and stacked with the phenylpyridine ligand containing N(211) and C(221). However, the pendant pyrazolylpyridine

with partially fluorinated ligands. Representative examples of luminescence spectra are given in Figure 4. Quantum yields varied from 0.08 (nonfluorinated $^{H}\mathbf{Ir}\cdot L$ series) to 0.31 ($^{CF3}\mathbf{Ir}\cdot L$ series). In all cases, there was modest rigidochromism with samples in a frozen MeOH/EtOH glass at 77 K having their emission maximum blue-shifted by 5—10 nm compared to emission in the fluid solution; this is associated with the charge-transfer

Table 4. Summary of the Photophysical Data for the Mononuclear Iridium(III) Complexes and Their Ir/Ln Adducts[a]

complex	λ_{em}/nm (RT)	Φ (RT)	τ/ns (RT)	λ_{em}/nm (77 K)	% Q (Gd)[b]	τ/ns (Gd adduct)[c]	% Q (Eu)[b]	τ/ns (Eu adduct)[c]
^{H}Ir·L^{pPh}	477	0.08	198	467	0	195 (94), 76 (6)	47	189 (77), 46 (23)
^{H}Ir·L^{mPh}	477	0.08	194	467	11	198 (76), 106 (24)	86	194 (23), 23 (78)
^{H}Ir·L^{pBiph}	477	0.08	196	467	0	213	11	172
^{H}Ir·L^{mBiph}	477	0.08	205	467	11	220 (90), 120 (10)	80	209 (12), 33 (88)
^{35}Ir·L^{pPh}	475	0.17	818	467	9	826	53	549
^{35}Ir·L^{mPh}	475	0.17	780	467	0	780	45	820 (57), 266 (43)
^{35}Ir·L^{pBiph}	475	0.17	916	467	22	908	75	306
^{CF3}Ir·L^{pPh}	481	0.31	1086	472	5	1163	33	727
^{CF3}Ir·L^{mPh}	481	0.31	961	472	5	1165	30	714 (60), 343 (40)
^{CF3}Ir·L^{pBiph}	481	0.31	1081	472	5	1146	25	670
^{CF3}Ir·L^{mBiph}	481	0.31	1071	472	5	1148	22	758
^{24}Ir·L^{pPh}	455	0.13	703	450	84	369 (90), 48 (8), 11(2)[d]	84	230 (57), 99 (25), 30 (19)[d]
^{24}Ir·L^{mPh}	455	0.13	698	450	47	478 (90), 180 (9), 12 (1)[d]	60	286 (98), 52 (2)[d]
^{24}Ir•L^{pBiph}	455	0.13	744	450	25	542 (70), 330 (27), 80 (3)[d]	71	307 (91), 51 (9)[d]
^{24}Ir·L^{mBiph}	455	0.13	759	450	59	561 (57), 293 (41), 22 (2)[d]	89	337 (86), 34 (14)[d]
^{245}Ir·L^{pPh}	452	0.17	1602	447	85	795 (56), 334 (39), 29 (5)[d]	73	508 (96), 67 (4)[d]
^{245}Ir·L^{mBiph}	452	0.17	1653	447	56	998 (54), 430 (44), 69 (2)[d]	86	408 (93), 39 (7)[d]

[a] All measurements were made in air-equilibrated CH_2Cl_2 at room temperature unless otherwise specified. Quantum yield measurements have an estimated uncertainty of ±20%. [b] Extent of quenching of the Ir-based emission intensity in the Ir/Ln dyad at the end of the titration with the appropriate $[Ln(hfac)_3(H_2O)_2]$. [c] Where one lifetime value is given, the decay fits satisfactorily to a single component (uncertainty ±10%); where two or three lifetime components are required to model the decay profile, the percent contribution of each to the total emission is given in parentheses (see the main text) and the uncertainties are larger. [d] For these Ir/Gd and Ir/Eu adducts, the presence of PET in addition to PEnT makes the decay kinetics particularly complicated and the presence of three components in some cases is necessary to achieve a reasonable fit; these lifetime values are not treated quantitatively in the main text because of their likely high uncertainty.
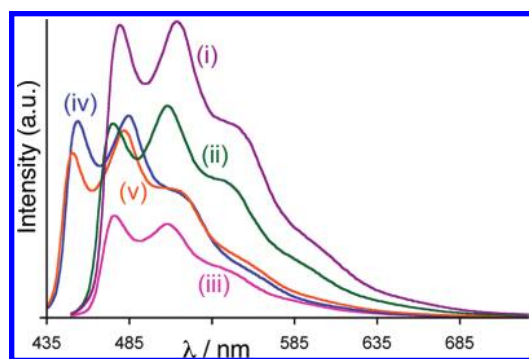

Figure 4. Luminescence spectra (CH_2Cl_2, room temperature) of (i) ^{CF3}Ir·L^{pPh}, (ii) ^{35}Ir·L^{pPh}, (iii) ^{H}Ir·L^{pPh}, (iv) ^{24}Ir·L^{pPh} and (v) ^{245}Ir·L^{pPh}. Solutions were isoabsorbing at the excitation wavelength such that differences in the emission intensities reflect differences in the quantum yields. Note the slightly lower energy emission for the first three cases compared to the last two.

Figure 5. Molecular structure of the complex cation of ^{245}Ir·L^{pPh}·Eu. Color scheme as for Figure 1. Thermal ellipsoids are at the 30% probability level.

unit is now part of the coordination sphere of an eight-coordinate {Eu(hfac)$_3$(diimine)} unit, which has an approximately square-antiprismatic geometry: one square face is formed by atoms N(131), N(142), O(622), and O(623) and the other by atoms O(422), O(423), O(522), and O(523). The Ir···Eu separation is 9.81 Å.

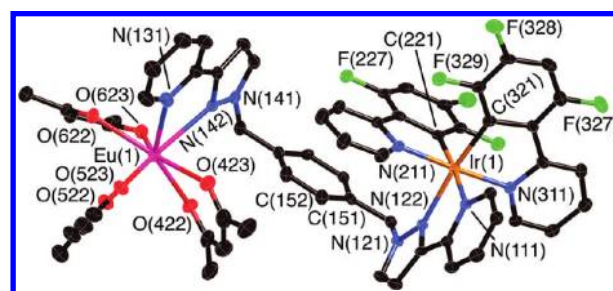**Photophysical Properties of Ir/Gd Dyads.** As described above, we performed a series of spectroscopic titrations in which portions of $Ln(hfac)_3 \cdot 2H_2O$ (Ln = Gd, Eu) were added to the mononuclear Ir·L complexes in CH_2Cl_2 until no further changes occurred to Ir-based emission. Formation of the dyads Ir·L·Ln resulted in no significant changes in the lowest-energy Ir-based MLCT absorptions, which extend out beyond 400 nm (any spectral changes to the Ir units at shorter wavelengths are masked by the strong absorption band associated with the diketonate units, which results in strong absorbance at wavelengths shorter than 370 nm). For luminescence measurements, we used excitation into this low-energy Ir-centered band at ca. 400 nm such that there could be no direct excitation of the {Ln(hfac)$_3$} units.

Conversion of mononuclear Ir·L complexes (typically ≈5 × 10^{-5} M^{-1} in a CH_2Cl_2 solution) to Ir·L·Gd dyads by titration
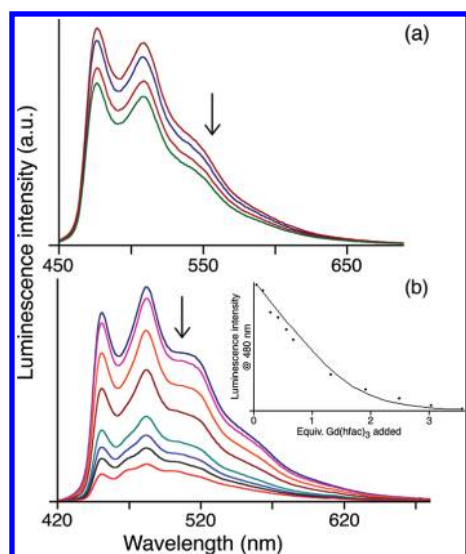
Figure 6. Changes in luminescence spectra recorded during titration of (a) ^{H}**Ir**$\cdot$**L**^{pPh} (5.9×10^{-5} M) and (b) ^{245}**Ir**$\cdot$**L**^{pPh} (7.8×10^{-5} M) with $[Gd(hfac)_3(H_2O)_2]$ in CH_2Cl_2 to form the respective **Ir**$\cdot$**L**$\cdot$**Gd** dyads. Note the much greater degree of quenching in the second case (see the main text for discussion). The concentration of the iridium complex was typically 10^{-4}–10^{-5} M; portions of $[Gd(hfac)_3(H_2O)_2]$ were added until there was no further change in Ir-based luminescence, which typically required the addition of <10 equiv. The inset to part b shows changes in the luminescence intensity at 480 nm as a function of added $[Gd(hfac)_3(H_2O)_2]$ and the fit of the data to a 1:1 binding isotherm (see the main text).

with $Gd(hfac)_3 \cdot 2H_2O$ in a CH_2Cl_2 solution resulted in some loss of intensity of Ir-based emission to an extent depending on the substituents on the phenylpyridine ligand attached to Ir^{III} (representative examples are given in Figure 6). The changes in the emission intensity during the titration fitted in all cases to a 1:1 binding isotherm, as expected, with an association constant of ca. 10^5 M^{-1} (the example shown in Figure 6b afforded $K_{ass} = 2 \times 10^5$ M^{-1}), which is typical for the formation of diimine adducts of this type in chlorinated solvents as per the equilibrium shown in Chart 1.[1a]

The complexes clearly split into two sets according to their photophysical behavior. The sets that have the slightly lower-energy Ir-based excited states, viz., based on ^{H}**Ir**, ^{35}**Ir**, and ^{CF3}**Ir**, all show little change in the Ir-based emission intensity when the **Ir**$\cdot$**L**$\cdot$**Gd** dyads form, with a modest degree of quenching (0–11% in most cases, with ^{35}**Ir**$\cdot$**L**$^{pBiph}\cdot$**Gd** showing 22% quenching); see Figure 6a for an example. This behavior is unremarkable and can reasonably be ascribed to changes in the vibrational behavior of the complexes when the bulky $\{Gd(hfac)_3\}$ unit binds such that nonradiative deactivation of the Ir-based excited state becomes slightly more favorable. Gd^{III} is incapable of acting as an energy acceptor from the excited states of these Ir units because its lowest excited state lies in the UV region (>30 000 cm^{-1}), hence its regular use as a control in experiments of this nature.

The other two series, ^{24}**Ir**$\cdot$**L**$\cdot$**Gd** and ^{245}**Ir**$\cdot$**L**$\cdot$**Gd**, show quite different behavior, with much more substantial quenching of Ir^{III}-based luminescence occurring (up to 85%; Figure 6b). In these two series, the excited state of the iridium(III) chromophore is significantly higher in energy [room temperature (RT) emission maxima at 452–455 nm] than in the first set (room temperature

emission maxima 475–481 nm), as shown in Figure 4 and Table 4. There is no reason why a higher-energy excited state should be much more effectively quenched by molecular vibrations,[12] which suggests that fundamentally different behavior is occurring.

The most likely possibility is that PET is occurring from the excited state of the Ir unit to the pyrazolylpyridine unit coordinated to $\{Gd(hfac)_3\}$ to give a short-lived Ir^{IV}/diimine$^{\bullet-}$ charge-separated state, providing a new quenching pathway. This is plausible given (i) the ease of oxidation of these complexes [we measured the Ir^{III}/Ir^{IV} couple to be in the range of 1.1–1.3 V vs Fc/Fc$^+$ for the fluorinated **Ir** complexes] and (ii) the well-known ability of diimine-type ligands to undergo one-electron reductions when coordinated to electropositive metal ions; for example, free 2,2′-bipyridine undergoes an irreversible reduction at −1.86 V vs NHE, which shifts to −1.26 V vs NHE in $[Ru(bipy)_3]^{2+}$.[13,14] We have observed this behavior before in an anthracenyl/Gd(diimine) dyad in which coordination of a $\{Gd(hfac)_3\}$ unit to the diimine made the diimine unit a sufficiently good electron acceptor to accept an electron from the excited state of the anthracene chromophore, generating a transient anthracenyl$^{\bullet+}$/diimine$^{\bullet-}$ excited state and quenching anthracene fluorescence.[15] Other Ir/Gd dyads recently published by us likewise show quenching of Ir-based emission for which we proposed the same explanation.[3g] We suggest that similar behavior is occurring in the ^{24}**Ir**$\cdot$**L**$\cdot$**Gd** and ^{245}**Ir**$\cdot$**L**$\cdot$**Gd** dyads, which have the highest-energy excited states of the series, and that this accounts for the greater quenching of Ir-based emission in those systems.

Time-resolved measurements of Ir-based emission support this idea: in all cases where the $\{Gd(hfac)_3\}$ unit causes significant quenching of the Ir unit (i.e., the "anomalous" ^{24}**Ir**$\cdot$**L**$\cdot$**Gd** and ^{245}**Ir**$\cdot$**L**$\cdot$**Gd** series), the decay profile of the residual luminescence is complex and can only be fitted to multiexponential decay with a minimum of three components, of which one is short (tens of nanoseconds). This is consistent with the presence of multiple conformers in solution that will have different rates of intercomponent PET. The shortest-lived components are on the time scale of a few tens of nanoseconds, 1–2 orders of magnitude shorter than luminescence of the free iridium complexes, indicative of electron-transfer rates on the order of 10^7–10^8 s^{-1} in these conformers. In all of these cases of multiexponential decay, the errors associated with the lifetime values for each component are much higher than usual and the data for these complexes in Table 4 should therefore not be overanalyzed, but the general behavior is clear. We note that, in some other conformationally flexible dyad molecules containing saturated components in the bridging ligands, we and others have likewise observed multiexponential decay kinetics associated with different molecular conformations.[16]

In clear contrast, the other three series ^{H}**Ir**$\cdot$**L**$\cdot$**Gd**, ^{35}**Ir**$\cdot$**L**$\cdot$**Gd**, and ^{CF3}**Ir**$\cdot$**L**$\cdot$**Gd**, where this behavior is not apparent, show much simpler time-resolved luminescence behavior, with a single component, or one dominant component, for Ir-based emission that is relatively little affected by the presence of the $\{Gd(hfac)_3\}$ unit. On this basis, we can be sure that the quenching of Ir-based luminescence in the ^{24}**Ir**$\cdot$**L**$\cdot$**Gd** and ^{245}**Ir**$\cdot$**L**$\cdot$**Gd** series is not due to a mechanical effect associated with binding of the $\{Gd(hfac)_3\}$ fragment or it would occur equally in all five series of complexes. This leaves a Ir* → (Gd-bound diimine) PET process in the series ^{24}**Ir**$\cdot$**L**$\cdot$**Gd** and ^{245}**Ir**$\cdot$**L**$\cdot$**Gd** as the most likely explanation for the strong quenching.[15]

Photophysical Properties of Ir/Eu Dyads. An exactly similar series of experiments, adding portions of $Eu(hfac)_3 \cdot 2H_2O$ to the **Ir·L** complexes (ca. 10^{-5} M in a CH_2Cl_2 solution) to generate dyads **Ir·L·Eu**, resulted in every case in partial quenching of Ir-based emission to an extent comparable to, or greater than, what was observed in the **Ir·L·Gd** dyads. Again, the complexes can be split into the same two sets. In the series ^{H}**Ir·L·Eu**, ^{35}**Ir·L·Eu**, and ^{CF3}**Ir·L·Eu**, whose gadolinium analogues showed relatively little quenching, the degree of quenching induced by the presence of Eu^{III} was much more substantial than that induced by Gd^{III}. This is to be expected if a new quenching pathway (Ir → Eu PEnT) becomes operative. For the other two series ^{24}**Ir·L·Eu** and ^{245}**Ir·L·Eu**, where quenching in the gadolinium(III) analogues was more substantial, the degree of quenching of the iridium luminophore induced by the presence of Eu^{III} is approximately comparable to what was induced by Gd^{III}, indicating that the additional PEnT process is not faster than the PET process, which will still be available.

In every case, the partial quenching of the Ir^{III} unit during titration with $Eu(hfac)_3 \cdot 2H_2O$ was accompanied by the appearance of sensitized emission from Eu^{III} in the form of the usual $^5D_0-^7F_n$ line series. Given that selective excitation of the iridium(III) chromophore was used, this sensitized emission can only arise from Ir → Eu EnT (either directly in the series ^{H}**Ir·L·Eu**, ^{35}**Ir·L·Eu**, and ^{CF3}**Ir·L·Eu** or indirectly via an initial electron-transfer step, as described above, in the series ^{24}**Ir·L·Eu** and ^{245}**Ir·L·Eu**). Two representative examples are shown in Figure 7; these are for the formation of ^{24}**Ir·L^{pPh}·Eu** (top) and ^{CF3}**Ir·L^{pPh}·Eu** (bottom). In the former case, the Ir-based emission intensity is 84% quenched in the dyad, whereas in the second, it is only 37% quenched, indicative of slower PEnT, which is less able to compete with radiative deactivation from the Ir^{III} excited state. In both sets of luminescence spectra, however, the rise in the intensity of the characteristic Eu^{III}-based emission lines as the titration proceeds, and the associated reduction in the intensity of Ir^{III}-based emission, which becomes partially quenched, are clear. This observation illustrates the general situation that the extent of Ir → Eu PEnT is (i) incomplete in solution[17] and (ii) highly variable. The PEnT rate will depend on electronic factors such as donor/acceptor spectroscopic overlap, which depends on the exact properties of the Ir^{III} donor because the acceptor is constant in every case, and electronic coupling, in the case of Dexter-type PEnT. It will also depend on steric factors, in particular the molecular conformation and intercomponent separation; and it will depend on the energy-transfer mechanism. This is a complex issue here because, in addition to the usual possibilities of Förster- and Dexter-type mechanisms for Ir → Eu PEnT,[1b] there is also the possibility of the initial electron-transfer step to generate a charge-separated Ir^{IV}/diimine$^{\bullet-}$ state (cf. the behavior of some of the Ir/Gd dyads) whose collapse by back electron transfer would provide the energy needed to sensitize Eu^{III}.[15] These issues are discussed in more detail in the next section.

The one set of data that does stand out is that in the ^{CF3}**Ir·L·Eu** series the extent of Ir → Eu PEnT is noticeably poorer than that in all of the other series, averaging only ca. 30% quenching of Ir-based emission across the series of four complexes with different bridging ligands. We suggest that this is due to the molecular conformation shown by the crystal structures (Figures 1−3). In all other series of complexes discussed here, with Ir cores having a different pattern of F-atom substituents, the phenylpyridine ligands are planar, and in every case, the crystal structures revealed a conformation in which the aromatic
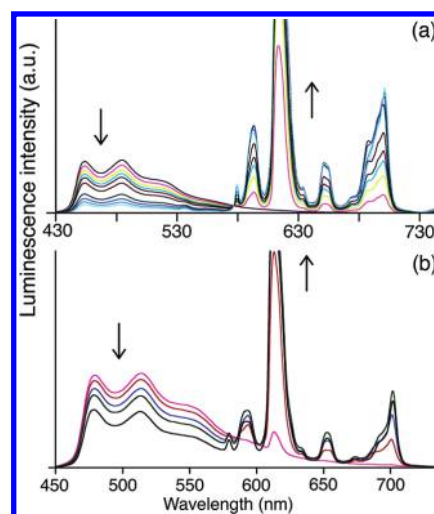

Figure 7. Changes in luminescence spectra recorded during titration of (a) ^{24}**Ir·L^{pPh}** (1.3×10^{-4} M) and (b) ^{CF3}**Ir·L^{pPh}** (4.8×10^{-5} M) with $[Eu(hfac)_3(H_2O)_2]$ in CH_2Cl_2 to form the respective **Ir·L·Eu** dyads. For typical conditions, see the caption to Figure 6. The most intense Eu-based emission peak at 615 nm is truncated to allow the rest of the spectra to be seen clearly.

core of the bridging ligand was engaged in π stacking with one of the phenylpyridine ligands (cf. Figures 1−3). This stacking is preserved in the structure of the dyad ^{245}**Ir·L^{pPh}·Eu** (Figure 5), implying that bonding of a $\{Ln(hfac)_3\}$ unit at the secondary pyrazolylpyridine site need not disturb this disposition of the bridging ligand, although more than one conformation in solution is, of course, likely, as mentioned above for the Ir/Gd dyads. Given the dominance of a Dexter-type pathway for PEnT, on the basis of our calculations (see below), we suggest that this aromatic stacking provides a pathway for weak intercomponent electronic coupling, which facilitates the PEnT process: the involvement of the phenylpyridine ligands in the excited state supports this. In contrast, the series ^{CF3}**Ir·L·Eu** provides the only cases in which no such π stacking is present because of the steric bulk of the CF_3 groups (cf. the crystal structure in Figure 3b,c) and the pendant aromatic groups of the bridging ligand L are not in close electronic contact with the coordinated phenylpyridine ligands, which participate in excited-state formation. Consequently, the PEnT process is less efficient, and quenching of the Ir donor by the $\{Eu(hfac)_3\}$ unit is diminished.

Time-resolved measurements show the same general picture, with more complicated decay kinetics for the ^{24}**Ir·L·Eu** and ^{245}**Ir·L·Eu** series, which required fitting to at least two and often three components. The other three series of dyads never required more than two components to get a good fit to the Ir-based luminescence decay kinetics, and in many cases, one component was sufficient. As mentioned earlier, the errors associated with extracting individual lifetimes, especially for minor components, of multiexponential decays are large, and the data should not be overinterpreted. We concentrate therefore on the ^{H}**Ir·L·Eu**, ^{35}**Ir·L·Eu**, and ^{CF3}**Ir·L·Eu** series for quantitative analysis of the energy-transfer rates.

We start with the ^{H}**Ir·L·Ln** series as a well-behaved example. The parent complex ^{H}**Ir·L^{pPh}** has an emission lifetime of 198 ns; in the dyad ^{H}**Ir·L^{pPh}·Gd**, at the end of the titration with $[Gd(hfac)_3(H_2O)_2]$, the emission has two components (195 and 76 ns), with the longer-lived component at the end of the

titration likely to arise from traces of free $^H\mathbf{Ir}\cdot L^{pPh}$, with no $\{Gd(hfac)_3\}$ bound.

In $^H\mathbf{Ir}\cdot L^{pPh}\cdot\mathbf{Eu}$, there are also two components to Ir-based luminescence decay with $\tau = 189$ and 46 ns. We can estimate the Ir $\rightarrow$ Eu EnT rate constant from eq 1, where τ_u is the "unquenched" emission lifetime of the Ir donor and τ_q is the partially quenched emission lifetime in the Ir/Eu dyad.

$$k_{EnT} = 1/\tau_q - 1/\tau_u \qquad (1)$$

The most obvious change in emission lifetimes is in the shorter-lived component in each case, which is reduced from 76 ns in $^H\mathbf{Ir}\cdot L^{pPh}\cdot\mathbf{Gd}$ to 46 ns in $^H\mathbf{Ir}\cdot L^{pPh}\cdot\mathbf{Eu}$. Using these figures, the value of k_{EnT} derived from eq 1 will reflect the additional quenching due to the possibility of Ir $\rightarrow$ Eu EnT, which is absent for the Ir/Gd dyads. Thus, we have $\tau_u = 76$ ns and $\tau_q = 46$ ns, affording an Ir $\rightarrow$ Eu energy-transfer rate constant, k_{EnT}, of 9×10^6 s^{-1}.

The pair of complexes $^H\mathbf{Ir}\cdot L^{mPh}\cdot\mathbf{Ln}$ (Ln = Gd, Eu) is similarly well-behaved, with lifetimes of 198 and 106 ns in the former case and 194 and 23 ns in the latter, with the 23 ns component dominating and only a small contribution from the 194 ns component (which probably just corresponds to a trace of free $^H\mathbf{Ir}\cdot L^{mPh}$). This gives a higher PEnT rate constant of 3.4×10^7 s^{-1}, consistent with a shorter Ir$\cdots$Eu separation because of the presence of a m-phenylene spacer rather than a p-phenylene spacer.

Likewise for $^H\mathbf{Ir}\cdot L^{mBiph}\cdot\mathbf{Eu}$, taking values for τ_q and τ_u of 33 and 120 ns (Table 4), we arrive at $k_{EnT} = 2.5 \times 10^7$ s^{-1}. For the final pair in this series, $^H\mathbf{Ir}\cdot L^{pBiph}\cdot\mathbf{Ln}$ (Ln = Gd, Eu), Ir-based luminescence from both could be fitted acceptably to single-exponential decay (213 and 172 ns, respectively). However, given the likelihood, based on the first three examples, of two (or more) lifetime components being present, it is likely that these are weighted average lifetime values for two similar luminescence components that cannot be deconvoluted; therefore, these numbers may not correspond to any single species, and using them for calculation of the EnT rates would be misleading. This leaves us with a set of three complexes in which the Ir $\rightarrow$ Eu energy-transfer rate constant can be calculated with confidence to be on the order of 10^7 s^{-1}.

The series $^{35}\mathbf{Ir}\cdot L\cdot\mathbf{Eu}$ is also readily interpretable in the same way and affords k_{EnT} values of 6.2×10^5 s^{-1}, 2.5×10^6 s^{-1}, and 1.4×10^6 s^{-1} via L^{pPh}, L^{mPh}, and L^{pBiph}, respectively; again we see that changing from L^{pPh} to L^{mPh}, which is expected to shorten the Ir$\cdots$Eu separation, increases the EnT rate constant, but changing L^{pPh} to the longer ligand L^{pBiph} also (and unexpectedly) increases k_{EnT}. Compared to the $^H\mathbf{Ir}\cdot L\cdot\mathbf{Eu}$ series, however, the k_{EnT} values are about an order of magnitude slower, with all being in the vicinity of 10^6 s^{-1}.

The series $^{CF3}\mathbf{Ir}\cdot L\cdot\mathbf{Ln}$ also provides readily interpretable luminescence lifetime data, and the time-resolved studies confirm the picture that was apparent from the steady-state measurements of intensity quenching, viz., that Ir $\rightarrow$ Eu PEnT is noticeably poor in this series because of the lack of aromatic stacking (cf. the crystal structures in Figure 3b,c). In all four cases, the parent iridium complex has a luminescence lifetime of ca. 1 μs, which $increases$ by about 10% in the $^{CF3}\mathbf{Ir}\cdot L\cdot\mathbf{Gd}$ adducts (despite the ca. 5% loss of the emission intensity in each case). In these cases, therefore, there is negligible PET to the $\{Gd-(diimine)\}$ fragment. In three of the four $^{CF3}\mathbf{Ir}\cdot L\cdot\mathbf{Eu}$ complexes (with L^{pPh}, L^{pBiph}, and L^{mBiph}), residual Ir-based emission shows

well-behaved single-exponential behavior with τ_q values of 727, 670, and 758 ns, respectively, affording from eq 1 k_{EnT} values of 5.2×10^5, 6.2×10^5, and 4.5×10^5 s^{-1}, respectively. For the remaining complex $^{CF3}\mathbf{Ir}\cdot L^{mPh}\cdot\mathbf{Eu}$, Ir-based emission had two components (714 and 343 ns): assuming that these correspond to different conformers of $^{CF3}\mathbf{Ir}\cdot L^{mPh}\cdot\mathbf{Eu}$, the k_{EnT} values are 5.4×10^5 and 2.1×10^6 s^{-1}, respectively. It is clear that across the same bridging ligands these Ir $\rightarrow$ Eu energy-transfer rates are at least an order of magnitude slower from the $^{CF3}\mathbf{Ir}$ unit than from the $^H\mathbf{Ir}$ unit, which has a more or less identical excited-state energy, and across the same bridging ligands, which we ascribe to the absence of aromatic stacking in the complexes and the consequent lack of electronic coupling between the components, which would inhibit PEnT if it operates by the Dexter mechanism.

Alternative estimates of the Ir $\rightarrow$ Eu PEnT rate constant, k_{EnT}, can be obtained from the observed reduction in the Ir-based emission intensity by using the following equation:

$$k_{EnT} = 1/\tau_u[(I_u/I) - 1] \qquad (2)$$

where τ_u is the luminescence lifetime of the unquenched donor and I_u/I is the ratio between the luminescence intensity of the unquenched donor, I_u, and the Ir-based luminescence intensity of the lanthanide adduct, I. As discussed above, the three series of dyads $^H\mathbf{Ir}\cdot L\cdot\mathbf{Eu}$, $^{35}\mathbf{Ir}\cdot L\cdot\mathbf{Eu}$, and $^{CF3}\mathbf{Ir}\cdot L\cdot\mathbf{Eu}$ showed only little (or no) Ir-based luminescence quenching upon binding to a $\{Gd(hfac)_3\}$ fragment, whereas substantial quenching was induced by binding to a $\{Eu(hfac)_3\}$ fragment. Thus, in these cases, we can consider that the observed donor luminescence quenching is due to Ir $\rightarrow$ Eu PEnT processes that sensitize Eu-based emission. By application of the equation above and by use of the values reported in Table 4 [% Q(Eu)], we obtain k_{EnT} values of 4.5×10^6, 1.4×10^6, and 4.5×10^5 s^{-1} for $^H\mathbf{Ir}\cdot L^{pPh}\cdot\mathbf{Eu}$, $^{35}\mathbf{Ir}\cdot L^{pPh}\cdot\mathbf{Eu}$, and $^{CF3}\mathbf{Ir}\cdot L^{pPh}\cdot\mathbf{Eu}$, respectively, involving the same bridging ligand (L^{pPh}) in each case. These values are similar to those obtained by lifetime analysis (vide supra) and, most importantly, they reflect the same trend in the series, with PEnT in the dyad $^{CF3}\mathbf{Ir}\cdot L^{pPh}\cdot\mathbf{Eu}$ being slowest because of the absence of aromatic stacking between the components as shown crystallographically.

The two series $^{24}\mathbf{Ir}\cdot L\cdot\mathbf{Eu}$ and $^{245}\mathbf{Ir}\cdot L\cdot\mathbf{Eu}$ again show more complex behavior (as did their gadolinium analogues) with at least two and sometimes three lifetime components for Ir-based emission. As discussed above, the properties of the $^{24}\mathbf{Ir}\cdot L\cdot\mathbf{Gd}$ and $^{245}\mathbf{Ir}\cdot L\cdot\mathbf{Gd}$ model complexes suggest that an initial electron-transfer step from the excited Ir unit to the diimine fragment coordinated to Gd^{III} is likely, and this will also be possible in the $^{24}\mathbf{Ir}\cdot L\cdot\mathbf{Eu}$ and $^{245}\mathbf{Ir}\cdot L\cdot\mathbf{Eu}$ series: trying to separate this from the additional contributions of Förster and Dexter energy transfer and the possible presence of different conformers, and come up with meaningful numbers for energy-transfer rates, is therefore not possible. We simply note that Ir $\rightarrow$ Eu PEnT also occurs in these dyads with substantial quenching of Ir-based emission (60–90%) by the Eu^{III} fragment and the associated appearance of sensitized Eu^{III} emission. On the basis of a comparison of luminescence intensities (eq 2), a similar conclusion is reached for the two series $^{24}\mathbf{Ir}\cdot L\cdot\mathbf{Eu}$ and $^{245}\mathbf{Ir}\cdot L\cdot\mathbf{Eu}$ because the luminescence quenchings induced by the formation of the gadolinium and europium adducts are comparable. Thus, the additional contribution of Förster or Dexter-type PEnT processes cannot be separated from the initial electron-transfer step and might be considered negligible.

11332

dx.doi.org/10.1021/ic2007759 |Inorg. Chem. 2011, 50, 11323–11339

Table 5. Parameters Used To Evaluate Possible Energy-Transfer Pathways within the Ir·L$^{\mathrm{pPh}}$·Eu Dyads

dyad	k_{EnT} (s^{-1})[a]	η_{EnT}	J_{F} (cm^3·M^{-1})	R_{c} (Å)	k_{F} (s^{-1})[b]	J_{D} (cm)	H (cm^{-1})[c]
$^{\mathrm{H}}$Ir·L$^{\mathrm{pPh}}$·Eu	44.8×10^5	0.47	2.69×10^{-20}	2.6	2.39×10^3	1.18×10^{-4}	0.18
^{35}Ir·L$^{\mathrm{pPh}}$·Eu	13.8×10^5	0.53	2.95×10^{-20}	3.0	1.35×10^3	1.25×10^{-4}	0.10
$^{\mathrm{CF3}}$Ir·L$^{\mathrm{pPh}}$·Eu	4.5×10^5	0.33	2.83×10^{-20}	3.3	1.78×10^3	1.12×10^{-4}	0.06
^{24}Ir·L$^{\mathrm{pPh}}$·Eu			2.76×10^{-20}	2.8	2.14×10^3	1.46×10^{-4}	
^{245}Ir·L$^{\mathrm{pPh}}$·Eu			2.73×10^{-20}	3.0	1.28×10^3	1.38×10^{-4}	

[a] Estimated from donor luminescence intensity quenching (see the text and eq 2). [b] Calculated for the stacked configuration at $d = 9.3$ Å (Figure 8). [c] This is the electronic coupling required for $k_{\mathrm{D}} = k_{\mathrm{EnT}}$, i.e., for the Dexter mechanism to dominate the EnT process.

Calculations of Possible Energy-Transfer Pathways. The nature of possible energy-transfer pathways in d/f dyads of this type has recently been reviewed.[1b] We consider initially the cases of Förster (dipole/dipole) EnT and Dexter-type EnT based on double electron exchange via bridging ligand orbitals.

The use of available spectroscopic quantities, i.e., the emission spectra of the Ir·L donor models and the absorption spectrum of the Eu^{3+} ion, allows us to calculate the spectral overlaps J_{F} and J_{D}. According to the Förster theory,[18] the critical radius, R_{c}, defined as the interchromophoric distance at which the Förster EnT rate constant, k_{F}, equals the intrinsic deactivation constant of the donor, $k_{\mathrm{in}} = 1/\tau_{\mathrm{u}}$, can be derived as well. The main parameters used to evaluate the EnT features in the Ir·L$^{\mathrm{pPh}}$·Eu dyads are summarized in Table 5: for calculations, we have concentrated on the series of complexes with the same bridging ligand L$^{\mathrm{pPh}}$.

The extremely small values obtained for J_{F} reflect the low interaction between emission (donor) and absorption (acceptor) dipoles, mainly due to the extremely small absorption coefficient of the Eu^{3+} ion ($\varepsilon_{\mathrm{max}} \approx 0.08$ M^{-1} cm^{-1}), which, in turn, result in a very short critical radius, R_{c}. According to the obtained R_{c} values, a distribution of EnT rate constants k_{F} can be calculated as a function of the interchromophoric distance d. Geometry optimization performed on the ^{245}Ir·L$^{\mathrm{pPh}}$·Eu and $^{\mathrm{CF3}}$Ir·L$^{\mathrm{pPh}}$· Eu complexes using molecular modeling[19] show the existence of minimum-energy structures (Figure 8) that nicely reproduce the crystal structures. In the more compact arrangement that occurs with those phenylpyridine ligands containing only nonhindering in-plane substituents (such as ^{245}Ir), we see a folded conformation with a π-stacking interaction between the phenylpyridine ligand and the central phenyl moiety of the bridge (Figure 8a), and the two metal centers are ca. 9.3 Å apart (cf. 9.8 Å in the crystal structure of ^{245}Ir·L$^{\mathrm{pPh}}$·Eu, vide infra). In contrast in the unfolded structure that is predicted for $^{\mathrm{CF3}}$Ir·L$^{\mathrm{pPh}}$·Eu, in which this π-stacking interaction is not sterically possible, this distance increases to ca. 13.3 Å (Figure 8b).

The EnT rate constants predicted by the Förster theory[18] (k_{F}) for these complexes, calculated for the shortest interchromophoric distance (taken as $d_{\mathrm{Ir-Eu}} = 9.3$ Å), are around 2×10^3 s^{-1}, i.e., 2 orders of magnitude lower than the experimentally observed rate constants (Table 5). Any greater values of $d_{\mathrm{Ir-Eu}}$ would reduce the k_{F} values still further. This definitely rules out any significant contribution of a PEnT transfer mechanism based on through-space dipole–dipole interactions; the calculated critical-transfer radius for PEnT by this mechanism is just ≈ 3 Å in all cases. In principle, higher-order multipolar contributions (e.g., dipole–quadrupole) can contribute to PEnT in cases where the dipole/dipole mechanism is inoperative because f–f transitions have significant transition quadrupole moments;[20] however, this has a higher (d^{-8}) distance dependence and, significantly, we
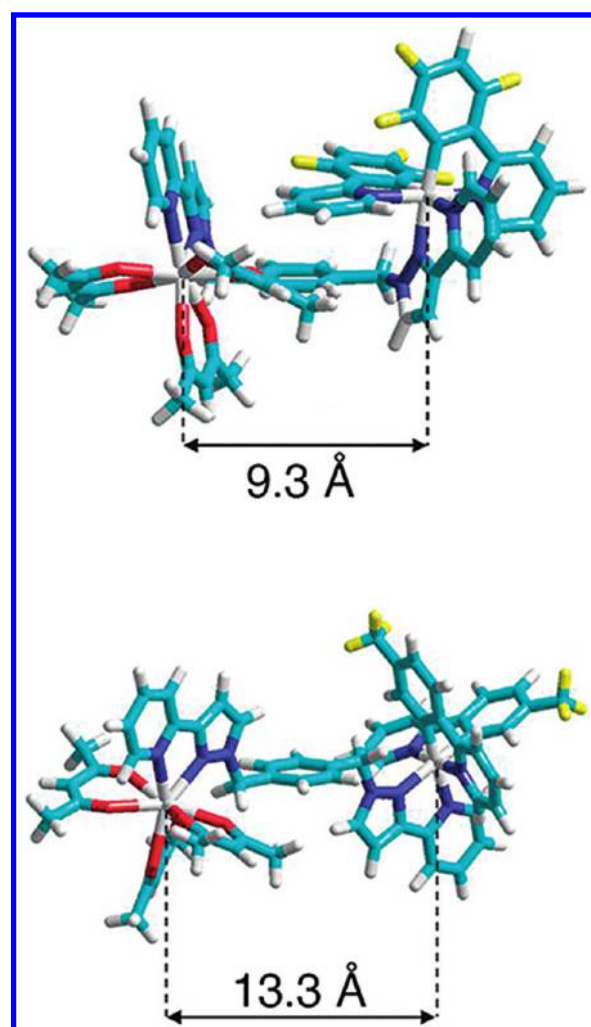

Figure 8. Results of molecular modeling studies showing minimum-energy conformations of (a) ^{245}Ir·L$^{\mathrm{pPh}}$·Eu and (b) $^{\mathrm{CF3}}$Ir·L$^{\mathrm{pPh}}$·Eu. Note that these are in good agreement with the crystal structures (vide supra), with the sterically hindering CF$_3$ group in the latter case resulting in a more extended conformation with no interligand stacking involving the phenylpyridine ligands.

were able to explicitly rule it out an earlier set of Ru$^{\mathrm{II}}$/Nd$^{\mathrm{III}}$ d/f dyads.[4]

In the case of the double-electron-exchange (Dexter-type) model,[21–23] the calculated overlap integrals, J_{D}, are on the order of 1×10^{-4} cm (Table 5) for all complexes. For this mechanism to be the dominant component of the Ir → Eu EnT process (i.e., for $k_{\mathrm{D}} = k_{\mathrm{EnT}}$), an electronic coupling term H of between 0.06
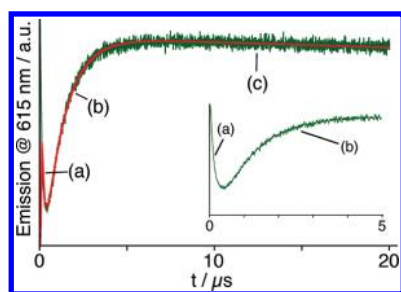
11333

dx.doi.org/10.1021/ic2007759 |*Inorg. Chem.* 2011, 50, 11323–11339

Figure 9. Time-resolved emission profile measured at 615 nm for $^{24}Ir \cdot L^{pPh} \cdot Eu$ in CH_2Cl_2 using 355 nm excitation. Note the three domains: (a) rapid decay of the residual Ir-based emission; (b) grow-in of Eu-based emission on the microsecond time scale; (c) normal slow decay of Eu-based emission (see the main text). The inset shows an expansion of the 0−5 μs region to make components a and b clearer.

and 0.18 cm^{-1} is necessary (Table 5). Such a modest electronic interaction might easily be provided by the $-CH_2-C_6H_4-CH_2-$ bridge connecting the two pyrazolylpyridine side ligands. It is interesting to note that on this basis we would expect the lowest H value to occur for $^{CF3}Ir \cdot L^{pPh} \cdot Eu$, where the presence of the bulky $-CF_3$ substituents on the phenylpyridine ligands prevents the π-stacked interaction observed in the other two complexes, $^{H}Ir \cdot L^{pPh} \cdot Eu$ and $^{35}Ir \cdot L^{pPh} \cdot Eu$, where the Ir → Eu EnT process is faster. As discussed above, this again implicates the role of the π interaction in making available an additional electronic communication pathway to facilitate the vectorial PEnT process.

We note that, although luminescence from Eu^{III} originates from the $^5D_0$ state, direct population of this level from the ground $^7F_0$ state is forbidden. The relevant selection rules are $|\Delta J| = 0, 1$ for Dexter-type energy transfer (with the specific case of $J = J' = 0$ being excluded, which applies to the $^5D_0 \leftarrow {}^7F_0$ transition) and $|\Delta J| = 2, 4, 6$ for multipolar energy transfer.[24] Although selection rules can be relaxed by various means, this issue still needs to be addressed when we consider the energy-transfer process. Accordingly, we performed time-resolved measurements at 615 nm—the peak of the Eu-based emission—for complex $^{24}Ir \cdot L^{pPh} \cdot Eu$ on the microsecond time scale. We could clearly identify (Figure 9) three different lifetime components at this wavelength. These are (i) a rapid decay of ca. 0.15 μs, corresponding to the weighted average of the rapid, multiexponential Ir-based decay at this wavelength (cf. Table 4), (ii) a slow increase with $\tau = 1.2$ μs, corresponding to a grow-in of the Eu-based emission intensity, and (iii) the expected slow Eu-based emission decay with $\tau = 0.65$ ms, typical for Eu^{III} emission in a nonprotic solvent.

The significant component here is the rise time of 1.2 μs for Eu-based emission. If the Eu^{III} ion were being excited directly into the emitting $^5D_0$ level by Ir → Eu PEnT, this rise time would match the rapid decay time of the Ir^{III} energy donor, yet it is much slower, implying the presence of an intermediate state. What we observe is entirely consistent with population of the $^5D_1$ level of Eu^{III}, which is fully allowed by Dexter-type energy transfer from the $^7F_0$ ground state (the selection rule requires that $\Delta J = 1$),[24] in agreement with our calculations suggesting that Dexter-type PEnT is feasible with only a very small electronic coupling required. It is known that nonradiative decay of the $^5D_1$ level of Eu^{III} to the emissive $^5D_0$ level is slow and occurs on a microsecond time scale,[25] so we are clearly observing Ir → Eu PEnT to the $^5D_1$ level of Eu^{III} on a time scale of $\approx 10^{-7}$ s
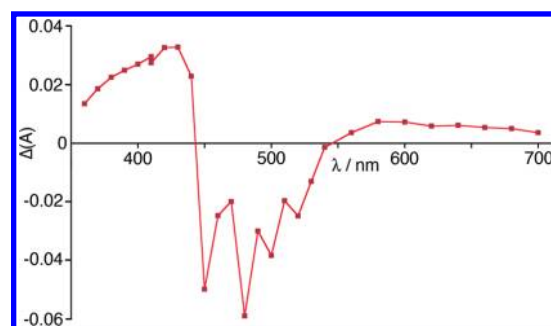

Figure 10. TA spectrum of $^{24}Ir \cdot L^{pPh} \cdot Gd$ in degassed CH_2Cl_2 at room temperature using 355 nm excitation, reconstructed from a global fit and corresponding to the spectrum of the component with a decay lifetime of 1.2 μs (see the main text). The spectra of $^{24}Ir \cdot L^{pPh}$ and $^{24}Ir \cdot L^{pPh} \cdot Eu$ are identical in appearance and differ only in their decay rates, pointing to a common excited state being observed in each case (see the main text).

(as calculated earlier), which is fully allowed by the Dexter mechanism, followed by slow nonradiative decay to the emissive $^5D_0$ level and subsequent luminescent decay. Importantly, all of the Ir energy donor units used in this work (Chart 1) have excited-state energies of >21000 cm^{-1} (Table 4), more than enough to populate the $^5D_1$ level of Eu^{III} (ca. 19 000 cm^{-1}) with no significant back energy transfer at room temperature.

Transient Absorption (TA) Measurements. For the systems where we have suggested that a PET step is operative, viz., the complex series $^{24}Ir \cdot L \cdot Gd$ and $^{245}Ir \cdot L \cdot Gd$ in which the presence of the {Gd(hfac)$_3$} fragment results in substantial quenching of Ir-based emission, we have performed TA measurements on representative members of the series to see if any evidence for a charge-separated Ir$^{IV} \cdots$(diimine$^{\bullet-}$)Gd intermediate could be found. The examples used were the free iridium complex $^{24}Ir \cdot L^{pPh}$ and its adducts $^{24}Ir \cdot L \cdot Gd$ and $^{24}Ir \cdot L \cdot Eu$ (Figure 10). The TA spectrum of $^{24}Ir \cdot L \cdot Gd$ is illustrated in Figure 10, but the spectra of free $^{24}Ir \cdot L^{pPh}$ and $^{24}Ir \cdot L \cdot Eu$ were essentially identical and Figure 10 can be used as a basis for the discussion of all three complexes.

First, the TA spectrum of $^{24}Ir \cdot L^{pPh}$ on its own was measured in deoxygenated CH_2Cl_2 using excitation at 355 nm. The result shows a new absorption at ca. 400 nm and a weaker region of new absorbance in the red region between 600 and 700 nm, which must be associated with the Ir-based excited state. The strong negative feature between 450 and 600 nm arises from intense stimulated emission from the Ir center. The decay of the excited-state absorptions monitored at various wavelengths gave a lifetime of 3.40 ($\pm$0.14) μs. We measured the emission lifetime of $^{24}Ir \cdot L^{pPh}$ in degassed CH_2Cl_2 for comparison purposes and obtained under these conditions dual-exponential decay with lifetime components of 2.33 ($\pm$0.05) and 3.36 ($\pm$0.05) μs, which we ascribe to different conformers of the flexible complex (cf. a value of 703 ns in $air-equilibrated$ CH_2Cl_2; Table 4).[26] These two components are sufficiently similar to one another that they are not resolved as separate components in the TA data, which have lower signal/noise ratios, but the agreement between these lifetimes and the value of 3.40 ($\pm$0.14) μs obtained from TA data confirms that the features in the TA spectrum are associated with the same excited state that generates luminescence.

In the presence of excess [Gd(hfac)$_3$(H$_2$O)$_2$], such that all of $^{24}Ir \cdot L^{pPh}$ was converted to $^{24}Ir \cdot L^{pPh} \cdot Gd$, the appearance of the

TA spectrum in deoxygenated CH_2Cl_2 is essentially identical (Figure 10) with the same regions of new absorption at ≈350−450 and 600−700 nm and the same negative emission peak (on which the characteristic vibrational fine structure of Ir-based emission is clearly resolved). All of this is consistent with formation of the normal Ir-based LC/MLCT excited state, and there are no additional features that can be ascribed to a separate charge-separated state. The kinetic behavior is different, however, with two lifetime components of 1.2 (±0.1) μs and 60 (±10) ns under these conditions, indicative of partial quenching by electron transfer, as discussed earlier. Luminescence decay obtained under the same conditions fits to three emission components with lifetimes of 1.43 (±0.05) μs, 0.56 (±0.02) μs, and 48 (±1) ns. Allowing for the poorer signal/noise ratio of the TA data, we can say that the 1.2 (±0.1) μs component obtained from TA data corresponds to an unresolved combination of the first two luminescence components, with the short components in each case [60 (±10) ns by TA and 48 (±1) ns by emission] also agreeing well with each other. Note that in the titration measurements involving the formation of ^{24}Ir·L^{pPh}·Gd in *air-equilibrated* CH_2Cl_2 we could resolve Ir-based emission components with lifetimes of 369 and 48 ns (Table 4).[26] Again, the presence of multiple decay components in Ir-based decay for ^{24}Ir·L^{pPh}·Gd is indicative of multiple conformations, with different Ir···Gd separations, being present.

The adduct ^{24}Ir·L^{pPh}·Eu in deoxygenated CH_2Cl_2 gave a TA spectrum nearly identical with that of ^{24}Ir·L^{pPh}·Gd, showing the signature of the Ir-based excited state. The two Ir-based lifetime decay components were 0.45 (±0.04) and 0.99 (±0.10) μs. Under the same conditions, time-resolved emission measurements showed two decay components with lifetimes of 0.37 (±0.01) and 0.76 (±0.03) μs, in reasonable agreement with the TA lifetimes (in aerated CH_2Cl_2, these are reduced to 99 and 230 ns; Table 4).[26] Any additional shorter-lived components in the TA spectrum that might be expected based on the data in Table 4 are too short to be detected with this setup. In this TA spectrum, we could also detect, as a contribution to the global fit, a weak negative feature at 615 nm corresponding to stimulated Eu-based emission (see the Supporting Information, Figures S1 and S2). However, the weakness of this and the relatively high signal-to-noise ratio precluded a detailed kinetic analysis at this wavelength, other than to observe that the rate of growth of this feature is approximately consistent with the 1.2 μs value for the rise time of Eu^{III}-based emission that was obtained from luminescence measurements (see earlier).

Thus, the TA spectra are showing in every case the signature of the Ir-based LC/MLCT excited state. If a charge-separated Ir^{IV}···(diimine$^{•−}$)Ln state is providing a quenching pathway in ^{24}Ir·L^{pPh}·Gd and ^{24}Ir·L^{pPh}·Eu (in addition to the direct energy transfer that operates in the latter complex), which seems likely,[15] then we cannot detect it by TA measurements. This implies that any charge-separated state is short-lived (<20 ns) because of rapid back electron transfer. If the forward electron-transfer process to generate the Ir^{IV}···(diimine$^{•−}$)Ln state in ^{24}Ir·L^{pPh}·Gd, which would be responsible for quenching of Ir-based emission, were also fast, we would not expect to see Ir-based emission components with lifetimes as long as 1.43 μs. The implication is that the charge-separated state is forming slowly because the gradient for forward PET is marginal. The observation of partially quenched lifetime components of 1.43 (±0.05) μs, 0.56 (±0.02) μs, and 48 (±1) ns in ^{24}Ir·L^{pPh}·Gd is ascribable to different PET rates in different conformers of the
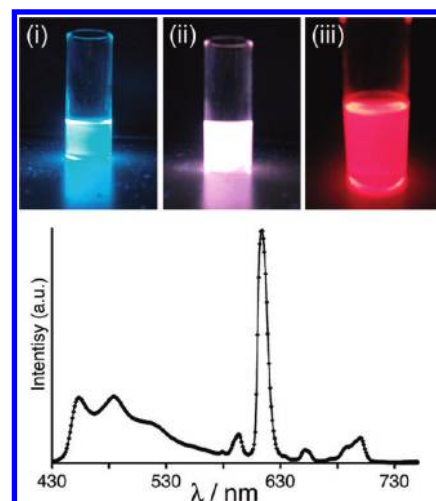
Figure 11. (a) Luminescence of samples of ^{24}Ir·L^{pPh} titrated with [Eu(hfac)$_3$(H$_2$O)$_2$] at different points during the titration: (i) pure ^{24}Ir·L^{pPh} showing the characteristic blue emission; (ii) after the addition of 0.1 equiv of [Eu(hfac)$_3$(H$_2$O)$_2$], i.e., a mixture containing ca. 90% ^{24}Ir·L^{pPh} and 10% ^{24}Ir·L^{pPh}·Eu; (iii) after the addition of 2 equiv of [Eu(hfac)$_3$(H$_2$O)$_2$] when the red Eu-based emission dominates. (b) Luminescence spectrum of the white-light-emitting mixture in part a(ii), i.e., recorded at the point during the titration when luminescence is closest to white.

flexible complex, but the charge-separated state is then decaying too quickly to detect with our instrument.

Balance of Blue and Red Luminescence Components To Give White Emission. As mentioned earlier, an appropriate balance of blue/green and red luminescence components has been used by several research groups to generate white-light emission from a single molecule,[7e,8a,8b] and we were interested in seeing if the same effect could be achieved using these Ir/Eu dyads. We found in every case that luminescence of these dyads quickly becomes dominated by the red component from the Eu^{III} center during the titration, i.e., as free Ir·L complex becomes converted to Ir·L·Eu. This is understandable on the basis of the very high quantum yield of red luminescence for [Eu(hfac)$_3$(diimine)] complexes in a CH_2Cl_2 solution (≥50% in some cases),[27] and the partial quenching of the Ir-based emission component in the Ir·L·Eu dyads, which will lead to loss of the blue component. We found that we could obtain good white-light emission from a sample of ^{24}Ir·L^{pPh} to which ≈0.1 equiv of Eu(hfac)$_3$(H$_2$O)$_2$ has been added, i.e., a mixture consisting of ca. 90% free ^{24}Ir·L^{pPh} and 10% of the dyad ^{24}Ir·L^{pPh}·Eu. The progression of the emission color from blue through white to red as this titration of Eu(hfac)$_3$(H$_2$O)$_2$ into ^{24}Ir·L^{pPh} proceeds is shown in Figure 11; at the point at which it is most white, the CIE coordinates are $x = 0.34$, $y = 0.32$.

In order to make a "pure" Ir·L·Eu dyad a better white-light emitter, it would be necessary to decrease the efficiency of the Ir → Eu EnT process such that, under selective excitation of the Ir component, the ratio of blue-to-red emission components is increased to give a better balance. In principle, this can be accomplished using ^{CF3}Ir as the donor because of the reduced Dexter EnT associated with the more open conformation, as discussed above. However, the altered pattern of substituents on the phenylpyridine ligands that slows down the PEnT process also shifts Ir-based emission to lower energy (^{24}Ir, $\lambda_{em} = 455$ nm; ^{CF3}Ir, $\lambda_{em} = 481$ nm) such that it no longer gives white light when

combined with the red from Eu-based emission. The closest that can be obtained, from an approximately 1:1 mixture of free $^{CF3}Ir \cdot L^{pBiph}$ and $^{CF3}Ir \cdot L^{pBiph} \cdot Eu$ that arises half-way through titration of $Eu(hfac)_3(H_2O)_2$ into $^{CF3}Ir \cdot L^{pBiph}$, is yellow in color (CIE coordinates $x = 0.37$, $y = 0.48$). The combination of the ^{24}Ir and $\{Eu(hfac)_3\}$ fluorophores to give white-light emission is clearly feasible, but correct balancing of the two components will require bridging ligands that give poorer Ir → Eu EnT; these studies are in progress.

■ CONCLUSIONS

A range of Ir/Eu dyads has been prepared in which an Ir^{III} unit with high-energy luminescence acts as an energy donor to Eu^{III} to generate sensitized luminescence following Ir → Eu energy transfer. The extent of energy transfer varies substantially between the different dyads because of changes in the intercomponent distance and the conformational flexibility of the molecules, with an energy-transfer efficiency of up to 90% occurring in some cases. There is a clear correlation of energy-transfer efficiency with the molecular conformation, as shown by crystallographic studies, with the majority of the dyads able to adopt a folded conformation in which the donor and acceptor components are indirectly linked by π stacking between ligand fragments. In the one series where this is sterically impossible, as confirmed by crystallography and also by calculation, the Ir → Eu energy-transfer efficiency is notably low. Multiexponential decay kinetics for Ir-based emission in the Ir/Eu dyads and the related Ir/Gd complexes can be ascribed to the presence of different conformers in solution.

In the related Ir/Gd dyads prepared as controls, two of the five series show surprisingly large quenching of Ir-based emission following binding of the $\{Gd(hfac)_3\}$ fragment, even though PEnT to Gd^{III} is not possible. We ascribe this to a PET process from the excited state of the iridium chromophore to the pendant diimine unit, which becomes easily reduced upon coordination to Gd^{III} to give a $Ir^{IV} \cdots (\text{diimine}^{\bullet -})Ln$ charge-separated state; however, this is too short-lived to be detected by nanosecond time scale TA spectra. This initial PET process could indirectly contribute to PEnT in the Ir/Eu dyads if the energy released by back electron transfer is sufficient to sensitize Eu^{III}.

Calculations of donor/acceptor spectroscopic overlap integrals for the Ir/Eu dyads and consideration of the requirements for Förster and Dexter-type energy transfer unambiguously show that Förster energy transfer is not possible over the distances involved, but Dexter-type energy transfer is possible provided a small electronic coupling across the bridging ligand is present, to which the aromatic π stacking observed in many of the crystal structures could contribute. The intermediacy of the Eu^{III} $^5D_1$ level as an initial energy acceptor, which has $\Delta J = 1$ from the ground state and whose population is therefore allowed by Dexter PEnT, is entirely consistent with this. Thus, Dexter-type PEnT is possible in all of the Ir/Eu dyads, and in two of the five series, an initial electron-transfer mechanism is also possible. An appropriate balance between the blue emission of the highest-energy iridium chromophores and the sensitized red Eu-based emission leads to white-light emission with CIE coordinates of $x = 0.34$, $y = 0.32$.

■ EXPERIMENTAL DETAILS

General Details. The following compounds were prepared according to published methods: the bridging ligands L^{pPh},[28] L^{mPh},[29] and L^{mBiph};[30] the dimers $[Ir(phpy)_2(\mu\text{-Cl})]_2$ based on unsubstituted 2-phenylpyridine and the various fluorinated analogues 2-(2,4-difluorophenyl)pyridine, 2-(3,5-difluorophenyl)pyridine, 2-(2,4,5-trifluorophenyl)-pyridine, and 2-[4-(trifluoromethyl)]phenylpyridine;[31] iridium(III) complexes $^{24}Ir \cdot L^{pBiph}$ and $^{35}Ir \cdot L^{pBiph}$;[3g] and $Eu(hfac)_3(H_2O)_2$.[32] The crystal structure of $[^{24}Ir \cdot L^{pBiph}] \cdot CHCl_3 \cdot H_2O$ (Figure 2b) was reported in an earlier communication[3g] but is also included here for completeness.

Electrospray mass spectrometry (ESMS) spectra were recorded using a Micromass LCT instrument; ^1H NMR spectra were recorded on a Bruker Avance-2 400 MHz instrument. UV/vis absorption spectra were measured on a Cary 50 spectrophotometer and luminescence spectra on a Jobin-Yvon Fluoromax 4 fluorimeter using air-equilibrated CH_2Cl_2 solutions at room temperature. Ir-based emission lifetimes derived from the luminescence titrations in Table 4 were measured using the time-correlated single-photon-counting technique with an Edinburgh Instruments "Mini-τ" luminescence lifetime spectrometer, equipped with a 405 nm pulsed diode laser as an excitation source and a Hamamatsu-H5773-03 photomultiplier tube (PMT) detector; the lifetimes were calculated from the measured data using the supplied software. Luminescence quantum yields (Φ in Table 4) were calculated by comparing areas of corrected luminescence spectra on an energy scale, from isoabsorbing solutions, following the method described by Demas and Crosby[33] and using fac-$[Ir(ppy)_3]$ (ppy = anion of 2-phenylpyridine) as a standard.[34]

Flash photolysis experiments were performed on a home-built setup. The samples were excited at 355 nm with the third harmonic (355 nm) of a Q-switched Nd:YAG laser LS-2137U (LOTIS TII). The energy of excitation pulses delivered to the sample was ca. 2.5 mJ, at 10 Hz repetition rate and 7 ns pulse width. A 150 W Xe arc lamp (Hamamatsu) was used as a probe light source. The probe light was detected through a SPEX MiniMate monochromator by a custom-built detector unit, based on a FEU-118 PMT. The detector current output was coupled into a Tektronix TDS 3032B digital oscilloscope and subsequently transferred to a computer. The same setup was used for the time-resolved emission measurements in the microsecond time domain, with the only difference being a blocked probe lamp.

All flash photolysis and microsecond time-resolved emission experiments were performed with the deoxygenated samples, degassed by the freeze−pump−thaw technique, and saturated with argon, unless noted otherwise. Quartz cells of 1 cm path length were used.

Analysis of the time-resolved data to obtain decay lifetimes was performed using *Igor Pro* software (WaveMetrics, Inc.). The decay kinetics were fitted to the exponential decay law using the least-squares algorithm built into *Igor Pro*. Global fitting was applied to analyze simultaneously the decay kinetics obtained for numerous spectral points, which enabled us to reconstruct the shape of TA spectra and considerably increase the reliability of the lifetime values.

Syntheses of Iridium(III) Complexes. All complexes were prepared in the same general way; the method described here for $^HIr \cdot L^{pPh}$ is typical. A solution of L^{pPh} (0.033 g, 85 μmol) was dissolved in dry CH_2Cl_2/MeOH (3:1, v/v) under N_2. To this was added a solution of $[Ir(phpy)_2(\mu\text{-Cl})]_2$ (0.040 g, 33 μmol) in the minimum amount of CH_2Cl_2. The mixture was stirred and heated to 50 °C overnight in the dark. The mixture was cooled to room temperature and the solvent removed under reduced pressure. A saturated aqueous KPF_6 solution (20 cm³) was added, and the resulting two-phase mixture was shaken vigorously and then separated; the aqueous residue was further extracted with several portions of CH_2Cl_2 (3 × 30 cm³). The combined organic fractions (containing the crude complex as its hexafluorophosphate salt) were dried using sodium sulfate, and the solvent was removed. The crude yellow powder was purified by column chromatography on silica gel using MeCN and 1% aqueous KNO_3; complex $^HIr \cdot L^{pPh}$ was the

11336

dx.doi.org/10.1021/ic2007759 |*Inorg. Chem.* 2011, 50, 11323–11339

second yellow band to come off the column. Fractions containing the pure product were combined and reduced in volume; excess KNO_3 was precipitated by the addition of CH_2Cl_2 and filtered off. Evaporation of the resultant solution to dryness afforded pure $^{H}Ir \cdot L^{pPh}$ as its nitrate salt. Characterization data are given below.

$^{H}Ir \cdot L^{pPh}$. ^1H NMR (400 MHz, $CDCl_3$): δ 8.68 (1H, d), 8.41 (1H, d), 8.06–7.99 (3H, m), 7.84 (1H, d), 7.79–7.67 (4H, m), 7.59–7.53 (2H, m), 7.52 (1H, d), 7.40–7.35 (2H, d), 7.26–7.21 (2H, m), 7.16–7.06 (3H, m), 7.02 (1H, d), 7.0–6.96 (1H, t), 6.87–6.79 (6H, m), 6.21 (1H, m), 6.01 (1H, d), 5.97 (2H, d), 5.29–5.25 (3H, m), 5.13 (1H, d). ESMS: m/z 893 (M + H$^+$). Anal. Calcd for $C_{46}H_{36}N_8IrNO_3 \cdot CH_2Cl_2$: C, 54.3; H, 3.7; N, 12.1. Found: C, 54.8; H, 3.7; N, 12.3.

$^{H}Ir \cdot L^{mPh}$. ^1H NMR (400 MHz, $CDCl_3$): δ 8.67 (1H, d), 8.33 (1H, d), 8.04–7.94 (3H, m), 7.84–7.68 (4H, m), 7.61–7.56 (3H, m), 7.48–7.43 (4H, m), 7.31–7.21 (3H, m), 7.09 (1H, t), 7.01–6.94 (4H, m), 6.9–6.82 (4H, m), 6.23 (1H, d), 6.11 (1H, s), 6.07 (1H, d), 5.90 (1H, d), 5.18–5.13 (3H, m), 5.01 (1H, d). ESMS: m/z 893 (M + H$^+$). Anal. Calcd for $C_{46}H_{36}N_8IrNO_3 \cdot CH_2Cl_2$: C, 54.3; H, 3.7; N, 12.1. Found: C, 54.1; H, 3.9; N, 11.8.

$^{H}Ir \cdot L^{pBiph}$. ^1H NMR (400 MHz, $CDCl_3$): δ 8.67 (1H, d), 8.49 (1H, d), 8.06 (1H, t), 8.00–7.96 (2H, m), 7.85 (1H, d), 7.80–7.66 (4H, m), 7.61–7.58 (2H, m), 7.53–7.44 (5H, m), 7.38–7.32 (3H, m), 7.28–7.08 (6H, m), 7.03–6.81 (6H, m), 6.30–6.26 (1H, m), 6.11–6.04 (3H, m), 5.47 (2H, s), 5.26 (1H, d), 5.09 (1H, d). ESMS: m/z 969 (M + H$^+$). Anal. Calcd for $C_{52}H_{40}N_8IrNO_3 \cdot 0.5H_2O \cdot 0.5 CH_2Cl_2$: C, 58.2; H, 3.9; N, 11.6. Found: C, 58.2; H, 3.7; N, 11.8.

$^{H}Ir \cdot L^{mBiph}$. ^1H NMR (400 MHz, $CDCl_3$): δ 8.63 (1H, d), 8.48 (1H, d), 8.06 (1H, t), 8.00 (1H, d), 7.94 (1H, d), 7.83 (1H, d), 7.76–7.66 (4H, m), 7.60–7.56 (3H, m), 7.44–7.18 (10H, m), 7.13–7.09 (2H, m), 7.01–6.92 (3H, m), 6.85–6.70 (4H, m), 6.26–6.20 (2H, m), 6.05–5.99 (2H, m), 5.48 (2H, s), 5.27 (1H, d), 5.16 (1H, d). ESMS: m/z 969 (M + H$^+$). Anal. Calcd for $C_{52}H_{40}N_8IrNO_3 \cdot 0.5CH_2Cl_2$: C, 58.7; H, 3.8; N, 11.7. Found: C, 59.1; H, 3.8; N, 11.7.

$^{24}Ir \cdot L^{pPh}$. ^1H NMR (400 MHz, $CDCl_3$): δ 8.68 (1H, d), 8.50 (1H, d), 8.24 (1H, d), 8.10 (2H, m), 8.01 (1H, d), 7.78 (2H, t), 7.68 (2H, t), 7.59–7.19 (9H, m), 7.00 (1H, d), 6.86 (3H, d), 6.51 (1H, dt), 6.41 (1H, dt), 5.96 (2H, d), 5.61 (1H, dd), 5.45 (1H, d), 5.27 (2H, s), 5.08 (1H, d). ESMS: m/z 965 (M + H$^+$). Anal. Calcd for $C_{46}H_{32}N_8F_4IrNO_3 \cdot CH_2Cl_2$: C, 50.8; H, 3.1; N, 11.3. Found: C, 50.4; H, 3.4; N, 11.5.

$^{24}Ir \cdot L^{mPh}$. ^1H NMR (400 MHz, $CDCl_3$): δ 8.65 (1H, br d), 8.45 (1H, d), 8.25 (1H, d), 8.09 (1H, t), 8.03 (1H, d), 7.91 (1H, d), 7.84–7.63 (6H, m), 7.56 (1H, d), 7.46–7.40 (2H, m), 7.32 (1H, t), 7.22 (2H, t), 7.08 (1H, t), 7.00–6.90 (3H, m), 6.58–6.46 (2H, m), 6.02 (1H, s), 5.97 (1H, d), 5.64 (1H, d), 5.46 (1H, d), 5.30 (1H, m), 5.18 (2H, s), 5.04 (1H, d). ESMS: m/z 965 (M + H$^+$). Anal. Calcd for $C_{46}H_{32}N_8F_4IrNO_3 \cdot CH_2Cl_2$: C, 50.7; H, 3.1; N, 11.3. Found: C, 50.3; H, 3.2; N, 11.3.

$^{24}Ir \cdot L^{pBiph}$. ^1H NMR (400 MHz, $CDCl_3$): δ 8.67 (1H, s), 8.59 (1H, d), 8.25 (1H, d), 8.15–8.11 (2H, m), 7.99 (1H, d), 7.83 (1H, t), 7.78–7.64 (5H, m), 7.53–7.22 (10H, m), 7.09 (2H, d), 7.01–6.97 (2H, m), 6.54 (1H, t), 6.46 (1H, t), 6.03 (2H, d), 5.68 (1H, d), 5.49–5.41 (4H, m), 5.12 (1H, d). ESMS: m/z 1041 (M + H$^+$). Anal. Calcd for for $C_{52}H_{36}N_8F_4IrNO_3 \cdot 0.5CH_2Cl_2$: C, 55.0; H, 3.2; N, 11.0. Found: C, 55.0; H, 3.3; N, 11.0.

$^{24}Ir \cdot L^{mBiph}$. ^1H NMR (400 MHz, $CDCl_3$): δ 8.64 (1H, s), 8.56 (1H, d), 8.25 (1H, d), 8.12 (1H, t), 8.07 (1H, d), 7.96 (1H, d), 7.83–7.74 (3H, m), 7.69–7.58 (4H, m), 7.41 (1H, t), 7.36–7.19 (9H, m), 7.06 (1H, t), 6.93 (1H, d), 6.72 (1H, t), 6.54 (1H, t), 6.33 (1H, t), 6.14–6.10 (2H, m), 5.65 (1H, m), 5.49–5.39 (4H, m), 5.18 (1H, d). ESMS: m/z 1041 (M + H$^+$). Anal. Calcd for $C_{52}H_{36}N_8F_4IrNO_3 \cdot CH_2Cl_2$: C, 53.6; H, 3.2; N, 10.6. Found: C, 54.0; H, 3.4; N, 10.9.

$^{245}Ir \cdot L^{pPh}$. ^1H NMR (400 MHz, $CDCl_3$): δ 8.69–8.65 (2H, m), 8.21–8.14 (3H, m), 8.00 (1H, d), 7.79–7.71 (4H, m), 7.56–7.21 (7H, m), 7.09 (1H, t), 6.99 (1H, d), 6.90 (2H, d), 6.83 (1H, t), 6.77–6.53

(2H, m), 6.02 (2H, d), 5.47 (1H, d), 5.28 (2H, s), 5.07 (1H, d). ESMS: m/z 1001 (M + H$^+$). Anal. Calcd for $C_{46}H_{30}N_8F_6IrNO_3 \cdot CH_2Cl_2$: C, 47.6; H, 2.7; N, 10.6. Found: C, 47.7; H, 2.7; N, 10.3.

$^{245}Ir \cdot L^{mBiph}$. ^1H NMR (400 MHz, $CDCl_3$): δ 8.69 (1H, d), 8.64 (1H, d), 8.22 (2H, m), 8.11 (1H, d), 7.94 (1H, d), 7.78–7.60 (6H, m), 7.56 (1H, d), 7.41 (1H, t), 7.36–7.20 (8H, m), 7.10–7.04 (2H, m), 6.92 (1H, d), 6.76–6.68 (2H, m), 6.51–6.45 (1H, m), 6.21–6.17 (2H, m), 5.47–5.43 (3H, m), 5.15 (1H, d). ESMS: m/z 1077 (M + H$^+$). Anal. Calcd for $C_{52}H_{34}N_8F_6IrNO_3 \cdot CH_2Cl_2$: C, 52.0; H, 3.0; N, 10.3. Found: C, 52.4; H, 3.3; N, 10.0.

$^{35}Ir \cdot L^{pPh}$. ^1H NMR (400 MHz, $CDCl_3$): δ 8.68 (1H, d), 8.57 (1H, d), 8.15–8.05 (3H, m), 7.82–7.73 (4H, m), 7.67–7.62 (3H, m), 7.38–7.24 (5H, m), 7.15 (1H, dt), 7.04 (1H, m), 6.92–6.83 (4H, m), 6.62 (1H, d), 6.38–6.29 (2H, m), 5.98 (2H, d), 5.49 (1H, d), 5.27 (2H, s), 5.15 (1H, d). ESMS: m/z 965 (M + H$^+$). Anal. Calcd for $C_{46}H_{32}N_8F_4IrNO_3 \cdot CH_2Cl_2$: C, 50.8; H, 3.1; N, 11.3. Found: C, 51.1; H, 3.4; N, 11.5.

$^{35}Ir \cdot L^{mPh}$. ^1H NMR (400 MHz, $CDCl_3$): δ 8.65 (1H, d), 8.54 (1H, d), 8.11 (1H, t), 8.02 (1H, d), 7.95 (1H, d), 7.77–7.72 (4H, m), 7.65–7.47 (4H, m), 7.39–7.21 (5H, m), 7.13 (1H, q), 7.02–6.88 (5H, m), 6.44–6.34 (2H, m), 6.15 (1H, s), 5.97 (1H, d), 5.30 (1H, d), 5.19 (2H, s), 5.04 (1H, d). ESMS: m/z 965 (M + H$^+$). Anal. Calcd for $C_{46}H_{32}N_8F_4IrNO_3 \cdot 0.5CH_2Cl_2 \cdot 0.5H_2O$: C, 51.8; H, 3.2; N, 11.7. Found: C, 51.9; H, 3.2; N, 12.1.

$^{35}Ir \cdot L^{pBiph}$. ^1H NMR (400 MHz, $CDCl_3$): δ 8.66 (2H, m), 8.16 (1H, t), 8.05 (1H, d), 7.98 (1H, d), 7.80–7.73 (5H, m), 7.61–7.52 (3H, m), 7.48 (2H, d), 7.43–7.20 (7H, m), 7.15 (3H, m), 7.00 (1H, t), 6.97 (1H, d), 6.86 (1H, d), 6.42 (1H, t), 6.36 (1H, t), 6.15 (2H, d), 5.48 (2H, s), 5.40 (1H, d), 5.12 (1H, d). ESMS m/z 1041 (M + H$^+$). Anal. Calcd for $C_{52}H_{36}N_8F_4IrNO_3 \cdot 0.5CH_2Cl_2$: C, 55.0; H, 3.2; N, 11.0. Found: C, 55.1; H, 3.4; N, 11.1.

$^{CF3}Ir \cdot L^{pPh}$. ^1H NMR (400 MHz, $CDCl_3$): δ 8.70 (1H, d), 8.50 (1H, d), 8.12–8.03 (3H, m), 7.93 (1H, d), 7.82 (2H, t), 7.75 (1H, d), 7.69 (1H, d), 7.63 (1H, d), 7.61–7.51 (3H, m), 7.40 (1H, d), 7.32–7.16 (6H, m), 7.08–6.99 (3H, m), 6.86 (2H, d), 6.30 (1H, s), 6.11 (1H, s), 5.90 (2H, d), 5.29–5.23 (3H, m), 5.07 (1H, d). ESMS: m/z 1029 (M + H$^+$). Anal. Calcd for $C_{48}H_{34}N_8F_6IrNO_3 \cdot CH_2Cl_2$: C, 50.1; H, 3.1; N, 10.7. Found: C, 50.5; H, 3.0; N, 11.1.

$^{CF3}Ir \cdot L^{mPh}$. ^1H NMR (400 MHz, $CDCl_3$): δ 8.65 (1H, d), 8.47 (1H, d), 8.10–8.05 (2H, m), 7.96–7.92 (2H, m), 7.85 (1H, t), 7.76–7.65 (4H, m), 7.61–7.50 (5H, m), 7.40 (1H, d), 7.29–7.21 (4H, m), 7.16–7.12 (2H, m), 6.99–6.96 (2H, m), 6.85 (1H, t), 6.33 (1H, s), 6.19 (1H, s), 6.05 (1H, s), 5.80 (1H, d), 5.18–5.14 (3H, m), 4.94 (1H, d). ESMS: m/z 1029 (M + H$^+$). Anal. Calcd for $C_{48}H_{34}N_8F_6IrNO_3 \cdot 0.5CH_2Cl_2$: C, 51.3; H, 3.2; N, 11.0. Found: C, 51.5; H, 2.8; N, 10.8.

$^{CF3}IrL^{pBiph}$. ^1H NMR (400 MHz, $CDCl_3$): δ 8.67 (1H, d), 8.60 (1H, d), 8.12 (1H, t), 8.08 (1H, d), 7.97 (2H, t), 7.87 (1H, t), 7.77–7.64 (5H, m), 7.60 (1H, d), 7.55–7.53 (2H, m), 7.40–7.38 (3H, m), 7.38–7.36 (3H, m), 7.31–7.10 (8H, m), 6.97 (1H, d), 6.39 (1H, s), 6.16 (1H, s), 6.05 (2H, d), 5.48 (2H, s), 5.23 (1H, d), 5.04 (1H, d). ESMS m/z 1105 (M + H$^+$). Anal. Calcd for $C_{54}H_{38}N_8F_6IrNO_3 \cdot 0.5H_2O \cdot 0.5CH_2Cl_2$: C, 53.7; H, 3.3; N, 10.3. Found: C, 53.5; H, 3.1; N, 10.5.

$^{CF3}Ir \cdot L^{mBiph}$. ^1H NMR (400 MHz, $CDCl_3$): δ 8.62–8.58 (2H, m), 8.11 (1H, t), 8.06 (1H, d), 7.96–7.80 (4H, m), 7.71–7.66 (3H, m), 7.61 (1H, d), 7.58 (1H, d), 7.43–7.36 (3H, m), 7.32–7.24 (6H, m), 7.22–7.16 (3H, m), 7.11 (1H, d), 6.97–6.91 (3H, m), 6.81 (1H, t), 6.38 (1H, s), 6.07 (1H, s), 6.02 (1H, s), 5.97 (1H, d), 5.49 (2H, s), 5.34 (1H, d), 5.11 (1H, d). ESMS: m/z 1105 (M + H$^+$). Anal. Calcd for $C_{54}H_{38}N_8F_6IrNO_3 \cdot H_2O \cdot 0.5CH_2Cl_2$: C, 53.3; H, 3.4; N, 10.3. Found: C, 53.5; H, 3.0; N, 10.0.

X-ray Crystallography. Crystals were removed from the mother liquor, coated with oil, and transferred to a stream of cold N_2 on the diffractometer as quickly as possible to prevent decomposition due to solvent loss. All structural determinations were carried out on a Bruker

11337

dx.doi.org/10.1021/ic2007759 |*Inorg. Chem.* 2011, 50, 11323–11339

SMART-APEX2 diffractometer using graphite-monochromated Mo Kα radiation ($\lambda = 0.710\,73$ Å) from a sealed tube source. After integration of the raw data and before merging, an empirical absorption correction was applied (*SADABS*)[35] based on a comparison of multiple symmetry-equivalent measurements. The structures were solved by direct methods and refined by full-matrix least squares on weighted F^2 values for all reflections using the *SHELX* suite of programs.[36] Pertinent crystallographic data are collected in Table 1; selected bond distances (from the metal coordination spheres) are given in Table 2. In general, the solutions and refinement were straightforward, although in some cases, scattering was weak because of one or all of (i) rapid desolvation of the crystal and loss of crystallinity, (ii) disorder of the anions and solvent molecules, and (iii) rotational disorder associated with the CF$_3$ groups; this necessitated the use of geometric restraints on disordered components and in some cases the use of isotropic thermal displacement parameters for particular atoms. Full details are given in the individual CIFs.

Calculation of Energy-Transfer Rates. For a general energy-transfer process, the intramolecular rate constant can be obtained from eq 1 (based on lifetime measurements) or eq 2 (based on emission intensity measurements); see the main text. The efficiency of the intramolecular energy-transfer process (η_{EnT}) can be evaluated by using eq 3:

$$\eta_{\mathrm{EnT}} = k_{\mathrm{EnT}}/(k_{\mathrm{EnT}} + k_{\mathrm{in}}) \tag{3}$$

in which $k_{\mathrm{in}} = 1/\tau_{\mathrm{u}}$, i.e., the intrinsic deactivation rate constant of the unquenched donor luminophore, and k_{EnT} was defined earlier.

For calculation of the energy-transfer rates based on the Förster and Dexter mechanisms, corrected donor-emission spectra and acceptor-absorption spectra on a wavenumber scale were used. Computations of the rate constants and the relevant spectroscopic overlap integrals were performed by using home-developed routines for *MATLAB 5.2* (The MathWorks, Inc.). The rate constant for energy transfer according to the Förster (k_{F}) and Dexter (k_{D}) mechanisms, respectively, were evaluated by employing eqs 4 and 5, respectively:

$$k_{\mathrm{F}} = 8.8 \times 10^{-25} \kappa^2 \varphi J_{\mathrm{F}}/n^4 \tau d^6 \tag{4}$$

$$k_{\mathrm{D}} = 4\pi^2 H^2 J_{\mathrm{D}}/h \tag{5}$$

in which $\kappa^2 = {}^2/_3$ is the statistical orientation factor, ϕ is the photoluminescence quantum yield of the donor, n is the refractive index of the solvent, τ is the excited-state lifetime of the donor, d is the donor—acceptor distance (taken as the metal—metal separation calculated from molecular modeling), H is the electronic coupling term, and h is Planck's constant. The spectral overlap integrals J_{F} and J_{D} were calculated from the emission spectrum of the donor, $D(\bar{\nu})$, and the acceptor absorption spectrum in molar absorptivity units, $A(\bar{\nu})$, by using eqs 6 and 7:

$$J_{\mathrm{F}} = \frac{\int D(\bar{\nu})\,A(\bar{\nu})/\bar{\nu}^4\,\mathrm{d}\bar{\nu}}{\int D(\bar{\nu})\,\mathrm{d}\bar{\nu}} \tag{6}$$

$$J_{\mathrm{D}} = \frac{\int D(\bar{\nu})\,A(\bar{\nu})\,\mathrm{d}\bar{\nu}}{\int D(\bar{\nu})\,\mathrm{d}\bar{\nu} \int A(\bar{\nu})\,\mathrm{d}\bar{\nu}} \tag{7}$$

Molecular Modeling. Optimized and fixed ground-state geometries in vacuo for the **Ir·L·Eu** complexes were obtained using the Sparkle-PM6 semiempirical quantum mechanical method[19a,b] with built-in parameters, as implemented in the *MOPAC 2009 for Windows* package,[19c] using the Gabedit GUI.[19d] An eigenvector following routine was used as the geometry optimization method, with a termination condition

set by the GNORM = 0.0 and DDMIN = 0.0 parameters. Cartesian coordinates for the two calculated structures shown in Figure 8 are in the Supporting Information (Tables S1 and S2).

■ ASSOCIATED CONTENT

ⓢ Supporting Information. X-ray crystallographic data in CIF format, flash photolysis information on **24Ir·L$^{\mathrm{PPh}}$·Eu** in degassed CH$_2$Cl$_2$, and coordinates for structures calculated by molecular modeling. This material is available free of charge via the Internet at http://pubs.acs.org.

■ AUTHOR INFORMATION

Corresponding Author
*E-mail: m.d.ward@sheffield.ac.uk.

■ ACKNOWLEDGMENT

■ DEDICATION

†Dedicated to our collaborator and colleague Francesco Barigelletti on the occasion of his retirement.

■ REFERENCES

(1) Reviews: (a) Ward, M. D. *Coord. Chem. Rev.* **2007**, *251*, 1663. (b) Ward, M. D. *Coord. Chem. Rev.* **2010**, *254*, 2634. (c) Chen, F. F.; Chen, Z.-Q.; Bian, Z.-Q.; Huang, C.-H. *Coord. Chem. Rev.* **2010**, *254*, 991. (d) Faulkner, S.; Natrajan, L. S.; Perry, W. S.; Sykes, D. *Dalton Trans.* **2009**, 3890.

(2) Representative recent examples: (a) Nonat, A. M.; Quinn, S. J.; Gunnlaugsson, T. *Inorg. Chem.* **2009**, *48*, 4646. (b) Ni, J.; Zhang, L.-Y.; Chen, Z.-N. *J. Organomet. Chem.* **2009**, *694*, 339. (c) Peng, G.; Qiu, Y.-C.; Liu, Z.-H.; Liu, B.; Deng, H. *Cryst. Growth Des.* **2010**, *10*, 114. (d) Eckes, F.; Bulach, V.; Guenet, A.; Strassert, C. A.; De Cola, L.; Hosseini, M. W. *Chem. Commun.* **2010**, *46*, 619. (e) Nonat, A. M.; Allain, C.; Faulkner, S.; Gunnlaugsson, T. *Inorg. Chem.* **2010**, *49*, 8449. (f) Kadjane, P.; Platas-Iglesias, C.; Ziessel, R.; Charbonniere, L. J. *Dalton Trans.* **2009**, 5688. (g) Li, X.-L.; Zhang, K.-J.; Li, J.-J.; Cheng, X.-X.; Chen, Z.-N. *Eur. J. Inorg. Chem.* **2010**, 3449.

(3) (a) Mehlstaubl, M.; Kottas, G. S.; Colella, S.; De Cola, L. *Dalton Trans.* **2008**, 2385. (b) Li, D.; Chen, F.-F.; Bian, Z.-Q.; Liu, Z.-W.; Zhao, Y.-L.; Huang, C.-H. *Polyhedron* **2009**, *28*, 897. (c) Chen, F.-F.; Bian, Z.-Q.; Lou, B.; Ma, E.; Liu, Z.-W.; Nie, D.-B.; Chen, Z.-Q.; Bian, J.; Chen, Z.-N.; Huang, C.-H. *Dalton Trans.* **2008**, 5577. (d) Chen, F.-F.; Bian, Z.-Q.; Liu, Z.-W.; Nie, D.-B.; Chen, Z.-Q.; Huang, C.-H. *Inorg. Chem.* **2008**, *47*, 2507. (e) Coppo, P.; Duati, M.; Kozhevnikov, V. N.; Hofstraat, J. W.; De Cola, L. *Angew. Chem., Int. Ed.* **2005**, *44*, 1806. (f) Tart, N. M.; Sykes, D.; Sazanovich, I.; Tidmarsh, I. S.; Ward, M. D. *Photochem. Photobiol. Sci.* **2010**, *9*, 886. (g) Sykes, D.; Ward, M. D. *Chem. Commun.* **2011**, *47*, 2279. (h) Lian, P.; Wei, H.; Zheng, C.; Nie, Y.; Bian, J.; Bian, Z. *Dalton Trans.* **2011**, *40*, 5476.

(4) Lazarides, T.; Sykes, D.; Faulkner, S.; Barbieri, A.; Ward, M. D. *Chem.—Eur. J.* **2008**, *14*, 9389.

(5) Parker, D. *Coord. Chem. Rev.* **2000**, *205*, 109.

(6) (a) Flamigni, L.; Barbieri, A.; Sabatini, C.; Ventura, B.; Barigelletti, F. *Top. Curr. Chem.* **2007**, *281*, 143. (b) Chen, Z.-Q.; Bian, Z.-Q.; Huang, C.-H. *Adv. Mater.* **2010**, *22*, 1534.

(7) (a) Mydlak, M.; Bizzarri, C.; Hartmann, D.; Sarfert, W.; Schmid, G.; De Cola, L. *Adv. Funct. Mater.* **2010**, *20*, 1812. (b) Orselli, E.; Kottas, G. S.; Konradsson, A. E.; Coppo, P.; Fröhlich, R.; De Cola, L; van Dijken, A.; Büchel, M.; Börner, H. *Inorg. Chem.* **2007**, *46*, 11082. (c) Sajoto, T.; Djurovich, P. I.; Tamayo, A. B.; Oxgaard, J.; Goddard, W. A.;

Thompson, M. E. *J. Am. Chem. Soc.* **2009**, *131*, 9813. (d) He, L.; Duan, L.; Qiao, J.; Wang, R.; Wei, P.; Wang, L.; Qiu, Y. *Adv. Funct. Mater.* **2008**, *18*, 2123. (e) Orselli, E.; Albuquerque, R. Q.; Fransen, P. M.; Fröhlich, R.; Janssen, H. M.; De Cola, L. *J. Mater. Chem.* **2008**, *38*, 4579.

(8) (a) Law, G.-L.; Wong, K.-L.; Tam, H.-L.; Cheah, K.-W.; Wong, W.-T. *Inorg. Chem.* **2009**, *48*, 10492. (b) He, G.-J.; Guo, D.; He, C.; Zhang, X.-L.; Zhao, X.-W.; Duan, C.-Y. *Angew. Chem., Int. Ed.* **2009**, *48*, 6132. (c) Kalinowski, J.; Cocchi, M.; Virgili, D.; Tattori, V.; Williams, J. A. G. *Adv. Mater.* **2007**, *19*, 4000.

(9) (a) Allain, C.; Faulkner, S. *Future Med. Chem.* **2010**, *2*, 339. (b) Bünzli, J.-C. G. *Chem. Rev.* **2010**, *110*, 2729. (c) Pandya, S.; Yu, J.-H.; Parker., D. *Dalton Trans.* **2006**, 2757.

(10) Natrajan, L. S.; Toulmin, A.; Chew, A.; Magennis, S. W. *Dalton Trans.* **2010**, *39*, 10837.

(11) Ward, M. D. *Chem. Commun.* **2009**, 4487.

(12) (a) Engelman, R.; Jortner, J. *Mol. Phys.* **1970**, *18*, 145. (b) Siebrand, W. *J. Chem. Phys.* **1967**, *47*, 2411. (c) Cummings, S. D.; Eisenberg, R. *J. Am. Chem. Soc.* **1996**, *118*, 1949.

(13) (a) Belser, P.; von Zelewsky, A. *Helv. Chim. Acta* **1980**, *63*, 1675. (b) Juris, A.; Balzani, V.; Barigelletti, F.; Campagna, S.; Belser, P.; von Zelewsky, A. *Coord. Chem. Rev.* **1988**, *84*, 85.

(14) We cannot directly measure the reduction potential of the pyrazolylpyridine unit coordinated to Gd^{III} in the **Ir·L·Gd** dyads because the competitive conditions required for electrochemical measurements (large excess of base electrolyte) would result in dissociation of the {Gd(hfac)$_3$} unit from the pyrazolylpyridine ligand.

(15) Lazarides, T.; Alamiry, M. A. H.; Adams, H.; Pope, S. J. A.; Faulkner, S.; Weinstein, J. A.; Ward, M. D. *Dalton Trans.* **2007**, 1484.

(16) (a) Easun, T. L.; Alsindi, W. Z.; Deppermann, N.; Towrie, M.; Ronayne, K. L.; Sun, X.-Z.; Ward, M. D.; George, M. W. *Inorg. Chem.* **2009**, *48*, 8759. (b) Easun, T. L.; Alsindi, W. Z.; Towrie, M.; Ronayne, K. L.; Sun, X.-Z.; Ward, M. D.; George, M. W. *Inorg. Chem.* **2008**, *47*, 5071. (c) Frank, M.; Nieger, M.; Vögtle, F.; Belser, P.; von Zelewsky, A.; De Cola, L.; Balzani, V.; Barigeletti, F.; Flamigni, L. *Inorg. Chim. Acta* **1996**, *242*, 281.

(17) In contrast, in a microcrystalline sample of ^{24}**Ir·L^{pPh}·Eu**, Ir-based emission is completely quenched and only the characteristic emission spectrum of europium(III) can be seen following excitation of the iridium(III) chromophore. However, in a condensed phase, additional quenching pathways can operate, and this is not directly comparable to behavior of molecules in a dilute solution.

(18) Förster, Th. *Discuss. Faraday Soc.* **1959**, *27*, 7.

(19) (a) Stewart, J. J. P. *J. Mol. Modeling* **2007**, *13*, 1173. (b) Freire, R. O.; Simas, A. M. *J. Chem. Theory Comput.* **2010**, *6*, 2019. (c) James, J. P.; Stewart *MOPAC2009*; Stewart Computational Chemistry: Colorado Springs, CO, 2008; http://OpenMOPAC.net. (d) Allouche, A.-R. *J. Comput. Chem.* **2011**, *32*, 174.

(20) (a) Scholes, G. D. *Annu. Rep. Phys. Chem.* **2003**, *54*, 57. (b) Malta, O. L. *J. Lumin.* **1997**, *71*, 229.

(21) Dexter, D. L. *J. Chem. Phys.* **1953**, *21*, 836.

(22) (a) One of the reviewers pointed out that pure Dexter PEnT is of necessity short range as it is predicated on direct orbital overlap between donor and acceptor components. However, the involvement of bridging ligand orbitals in a superexchange process can extend the effective range over which the double-electron exchange can occur, and PEnT involving a superexchange process across extended bridging ligands is often referred to as Dexter-type [see refs 4 and 22b,c for examples]. Superexchange between d- and f-block ions across a bridging ligand has been the subject of theoretical analysis in a Cr^{III}/Yb^{III} system (ref 23). (b) Schlike, B.; Belser, P.; De Cola, L.; Sabbioni, E.; Balzani, V. *J. Am. Chem. Soc.* **1999**, *121*, 4207. (c) Benniston, A. C.; Harriman, A.; Li, P.; Sams, C. A. *J. Am. Chem. Soc.* **2005**, *127*, 2553.

(23) Mironov, V. S.; Chibotaru, L. F.; Ceulemans, A. *Phys. Rev. B* **2003**, *67*, 014424.

(24) (a) de Sá, G. F.; Malta, O. L.; de Mello Donegá, C.; Simas, A. M.; Longo, R. L.; Santa-Cruz, P. A.; da Silva, E. F., Jr. *Coord. Chem. Rev.* **2000**, *196*, 165. (b) Hebbink, G. A.; Grave, L.; Woldering, L. A.; Reinhoudt, D. N.; van Veggel, F. C. J. M. *J. Phys. Chem. A* **2003**, *107*, 2483.

(c) Gonçalves e Silva, F. R.; Malta, O. L.; Reinhard, C.; Güdel, H.-U.; Piguet, C.; Moser, J. E.; Bünzli, J.-C. G. *J. Phys. Chem. A* **2002**, *106*, 1670.

(25) (a) Nardi, E.; Yatsiv, S. *J. Chem. Phys.* **1962**, *37*, 2333. (b) Bhaumil, M. L.; Nugent, L. J. *J. Chem. Phys.* **1965**, *43*, 1680. (c) Buono-Core, G. E.; Li, H.; Marciniak, B. *Coord. Chem. Rev.* **1990**, *99*, 55. (d) Zhao, X.; Fei, H.; Tian, K.; Li, T. *J. Lumin.* **1988**, *40−41*, 286.

(26) The luminescence lifetimes obtained in deoxygenated CH_2Cl_2 are longer than those obtained for the same compounds during the titration studies in air-equilibrated CH_2Cl_2 (Table 4), which is typical behavior associated with the absence of quenching of a triplet excited state by $^3O_2$.

(27) (a) De Silva, C. R.; Maeyer, J. R.; Wang, R.; Nichol, G. S.; Zheng, Z. *Inorg. Chim. Acta* **2007**, *360*, 3453. (b) Osawa, M.; Hoshino, M.; Wada, T.; Hayashi, F.; Osanai, S. *J. Phys. Chem. A* **2009**, *113*, 10895. (c) Hasegawa, Y.; Yamamuro, M.; Wada, Y.; Kanehisa, N.; Kai, Y.; Yanagida, S. *J. Phys. Chem. A* **2003**, *107*, 1697.

(28) Argent, S. P.; Adams, H.; Riis-Johannessen, T.; Jeffery, J. C.; Harding, L. P.; Ward, M. D. *J. Am. Chem. Soc.* **2006**, *128*, 72.

(29) Argent, S. P.; Adams, H.; Harding, L. P.; Ward, M. D. *Dalton Trans.* **2006**, 542.

(30) Paul, R. L.; Couchman, S. M.; Jeffery, J. C.; McCleverty, J. A.; Reeves, Z. R.; Ward, M. D. *Dalton Trans.* **2003**, 845.

(31) (a) Sprouse, S.; King, A. K.; Spellane, P. J.; Watts, R. J. *J. Am. Chem. Soc.* **1984**, *106*, 6647. (b) Coppo, P.; Plummer, E. A.; De Cola, L. *Chem. Commun.* **2004**, 1774. (c) Ragni, R.; Plummer, E. A.; Brunner, K.; Hofstraat, J. W.; Babudri, F.; Farinola, G. M.; Naso, F.; De Cola, L. *J. Mater. Chem.* **2006**, *16*, 1161.

(32) Richards, M. F.; Wagner, W. F.; Sands, D. E. *J. Inorg. Nucl. Chem.* **1968**, *30*, 1275.

(33) Demas, J. N.; Crosby, G. A. *J. Phys. Chem.* **1971**, *75*, 991.

(34) (a) Namdas, E. B.; Ruseckas, A.; Samuel, I. D. W. *J. Phys. Chem. B* **2004**, *108*, 1570. (b) King, K. A.; Spellane, P. J.; Watts, R. J. *J. Am. Chem. Soc.* **1985**, *107*, 1431.

(35) Sheldrick, G. M. *SADABS: A program for absorption correction with the Siemens SMART system*; University of Gottingen: Gottingen, Germany, 1996.

(36) Sheldrick, G. M. *Acta Crystallogr., Sect. A* **2008**, *64*, 112.